

Revolutionary valorization of carbon dioxide into dimethyl carbonate is catalyzed by sodium chloride: cheap, clean, one-pot, and water-free synthesis

Vitaly V. Chaban,¹ Nadezhda A. Andreeva,² Leonardo Moreira dos Santos,³ and Sandra Einloft^{3,4}

(1) Yerevan State University, Yerevan, 0025, Armenia. E-mail: vvchaban@gmail.com.

(2) Peter the Great St. Petersburg Polytechnic University, Saint Petersburg, Russian Federation.

(3) School of Technology, Pontifical Catholic University of Rio Grande do Sul - PUCRS, Porto Alegre Brazil.

(4) Post-Graduation Program in Materials Engineering and Technology, School of Technology Pontifical Catholic University of Rio Grande do Sul – PUCRS, Brazil.

Abstract:

The robust valorization of carbon dioxide (CO₂) stays at the center of sustainable development. Since CO₂ represents a low-energy compound, its transformation into commercially coveted products is cumbersome. In the present work, we report a revolutionary method to obtain dimethyl carbonate (DMC) out of methanol (CH₃OH) and CO₂ catalyzed by sodium chloride (NaCl) and similar inorganic salts. The computational exploration revealed a mechanism of favorable catalysis, which was subsequently confirmed experimentally. Unlike all competitive syntheses of DMC, the new one does not produce water and, therefore, the hydrolysis of a carbonate does not occur. No dehydrating agents are necessary. The employed catalyst is cheap and permanently exists in the same phase with the reactants and products. The action of NaCl was compared to those of other alkali metal salts, LiI, LiCl, and KI, and competitive performances were recorded. The experimentally obtained result outperforms most competing technologies according to the DMC yield, 19% with molecular sieves and 17% without molecular sieves. All existing competitors are excelled by the simplicity and cleanness of the synthesis. The reported

advance substantially simplifies the synthesis of linear organic carbonates and robustly valorizes CO₂.

Keywords:

Dimethyl carbonate; carbon dioxide utilization; sodium chloride; methanol.

TOC Image

Sodium chloride makes the production of dimethyl carbonate way more straightforward.



1. Introduction

The extra concentration of carbon dioxide (CO₂) in the atmosphere of the Earth is seen as a factor leading to emerging global warming.¹ The peak average yearly temperatures were recorded during the last several years. Furthermore, the steady large-scale temperature increase, allegedly, happens for more than a century. The time frame somehow coincides with the boom of large-scale chemical technologies. These global changes reflect undesirable climate modifications, the thawing of glaciers, unpredictable and unstable evolutions of the existing ecosystems. The sustainable development of humanity implies that current CO₂ concentration is monitored and on-time measures are taken to stabilize it.¹ More and more advanced fixation and conversion of greenhouse gases is pursued worldwide²⁻⁶ by adapting novel materials and approaches.⁷⁻¹⁰

CO₂ represents one of the most thermodynamically stable molecules composed of carbon and oxygen. Therefore, it appears to be chemically challenging to design novel energetically favorable reactions involving CO₂ as a reactant. In the meantime, CO₂ is not just an environmental hazard for people but also a valuable source of carbon for building live creatures and accumulating energy, e.g., in the form of starch. Live nature organisms, such as plants and bacteria, learned to rather efficiently apply CO₂ in photosynthesis to produce carbohydrates. Furthermore, certain bacteria elaborated the noteworthy chemical pathways to valorize this greenhouse gas into methanol (CH₃OH) and other small organic molecules. Teaching microbes to produce aqueous ethanol solutions out of CO₂ is definitely the next worthwhile educational challenge for microbiologists. The already-known versatility of the sophisticated CO₂ chemistry around us is noteworthy, notwithstanding its obvious thermodynamic stability.¹¹ Similar to solar energy, CO₂ is an abundant and virtually free resource for our civilization. The robust valorization of CO₂ represents the means to create a more sustainable economy and mitigate adverse changes in the planetarian climate.

The two major sources of greenhouse gases are the burning of fossil fuels (mainly CO₂) and agriculture (mainly CH₄). Animals persistently exhale CO₂. Finding routes to either employ CO₂ and CH₄ directly or synthesize valuable products out of them would be an essential step toward sustainability. In pure state, CO₂ can be used as a refrigerant, propellant, and fire extinguisher. In chemical technologies, CO₂ is a reactant to produce fuels, plastics, and task-specific chemicals, such as alcohols, carboxylic acids, dialkyl, and cyclic organic carbonates. The industry of CO₂ valorization remains in its early stages. As it develops, new jobs in chemical and manufacturing industries will emerge and innovative products may be proposed. The perspective of using CO₂ as a feedstock for new products deserves a profound investigation nowadays.¹²

Organic and inorganic carbonates are genetically close to CO₂.¹³⁻¹⁶ Carbonates can be arguably seen as condensed/trapped CO₂.¹⁷ Mineralization designates a process, in which carbonate-containing minerals are derived out of CO₂. These products are versatile construction materials.¹⁸⁻²⁰ In the form of inorganic carbonates, the captured volumes of CO₂ can be stored for, at least, centuries. In turn, organic linear and cyclic carbonates can be obtained via the reactions of CO₂ with alcohols or epoxides. Organic carbonates are important solvents for applications.²¹⁻²⁶ They are conventionally used in mixtures with more polar solvents to tune the dielectric constants of the liquid media.²⁷⁻³⁰ Whatever technology is chosen for CO₂ valorization, it is of paramount importance that the ultimate products be commercially competitive. This criterion means that all stages of the chemical transformations responsible for valorization must demand adequate amounts of energy, catalysts, and co-reactants.

In the present work, we boost the valorization of CO₂ to obtain dimethyl carbonate (DMC). CH₃OH acts as a co-reactant in this synthesis. Whereas this is a vivid field of research, the achieved progress has been fairly modest thus far.³⁴⁻⁴² The developed catalysts partly eliminate the high activation barrier to generate methoxy moieties by deprotonating CH₃OH molecules. Furthermore, the thermochemistry of the entire reaction is generally unfavorable.^{14,31-33} As a result, most

published works report the DMC yields of 5-15 mol%, notwithstanding extreme conditions of the synthesis (up to 180 degrees Celsius and up to 300 bar) and the need to dehydrate samples.^{18,31,34-}

36

d-Metal oxides distributed over suitable inorganic matrices are presently used to abstract the proton from CH₃OH.³¹ For instance, Fe₃O₄, CeO₂, ZnO, ZrO₂, TiO₂, La₂O₃, MgO, Al₂O₃, SnO₂, CuO, CuNi, TiO₂, FeO, and numerous noteworthy catalytic setups^{14,36-44} were employed under various reaction conditions to enhance the selectivities and conversions of CH₃OH. As a rule, more chemically active metals exhibit better performances but morphologies of the resulting catalysts and matrices are also very essential. The metal atom coordinates the hydroxyl group of CH₃OH and polarizes the oxygen-hydrogen bond. The oxygen atom of the catalyst does the same with the hydroxyl hydrogen. The elongated covalent bond in hydroxyl helps the proton to dissociate. The proton abstraction represents the rate- and yield-limiting stage of the reaction. Another problem of the existing approaches is the formation of water, which hydrolyzes DMC.⁴⁵ The dehydrating agents are employed to combat the reverse reaction. Such a circumvention improves the yields but essentially complicates the experimental setups making the results hard to interpret and rationalize.⁴⁵

Herein, we abandoned metal oxides and trialed alkali metal salts – NaCl, KI, LiI – as catalysts. Unlike competitors, the latter are soluble in CH₃OH. The cations coordinate CH₃OH molecules strongly. Thus, the total surface of contact between the catalyst and the reactants is maximized and their usage gets more efficient. CH₃OH can be supplied in liquid or gaseous states. CO₂ is permanently in the gaseous state. The elevated pressure accelerates the reaction and improves the thermochemistry thanks to suppressing the entropic penalty. To initiate the conversion of CH₃OH, the methoxy group, CH₃O*, must first be formed. The role of the dissolved inorganic ions is to stretch the hydroxyl moiety of CH₃OH, thus promoting hydrogen abstraction upon thermal motion. The inorganic anion (chloride, iodide) thermodynamically stabilizes the

abstracted proton. Simultaneously, CH_3O^* readily forms the covalent bond with CO_2 , which transforms into the carboxyl moiety, giving $\text{CH}_3\text{OC}(\text{O})\text{O}^-$. The alkali cation or the abstracted proton temporarily coordinates the new anion due to the Coulombic attraction. The reaction is finalized via the attachment of the methyl group, which comes from the promoter molecule, $\text{CH}_3\text{OC}(\text{O})\text{O}^- + \text{CH}_3\text{I} = \text{DMC} + \text{I}^-$. The liberated iodide stabilizes the excess proton. Most importantly, the above-described route does not involve water, the most undesirable by-product in all competitor formulations. The computational investigation has been concentrated on the most energetically demanding transformation, whereas the synthesis has included all essential experimental descriptors of the aggregate reaction and verified the theoretical predictions.

2. Computational methodology

The simulated systems were composed of three CH_3OH molecules, one of which is a reactant and two of which are solvents. The catalyst was represented as a single ion pair (NaCl , LiI , and KI). One CO_2 molecule was located nearby. The described chemical compositions were immersed into a polarizable continuum with the physicochemical properties of CH_3OH .

The work makes use of numerous computational methods, such as local optimization to the closest stationary point (local minimum and transition state),⁴⁶⁻⁴⁸ potential energy landscape exploration along the chosen reaction coordinates, global minimum configuration search, single-point calculations using semiempirical⁴⁹⁻⁵⁰ and hybrid density functional theory (HDFT) Hamiltonians,⁵¹ Born-Oppenheimer PM7-MD simulations,⁵²⁻⁵⁵ thermochemistry, and reaction activation barrier evaluations. The following paragraphs characterize the parameters of the methods, that were employed, and argue the methodological choices.

The reported geometries and electronic properties of the reactants, products, and transition states were obtained in the framework of HDFT. The exchange-correlation, range-separated, meta-

general-gradient-approximation functional M11 was employed to obtain electronic structures.⁵¹ The self-consistent-field convergence criterion of 10^{-8} hartree was applied. The empirical correction to account for the longer-range attractive forces (dispersion) acting among non-covalently bound atoms was applied on the fly. The split-valence triple-zeta polarized basis set TZVP was used⁵⁶ to supply elementary functions describing electronic orbitals of chemical elements, out of which the molecular wave function was constructed for each simulated system.

The PM7 Hamiltonian was employed to conduct a global potential energy minimum search for the structures of chemical interest (reactants and products) and molecular dynamics simulations.⁴⁹⁻⁵⁰ The latter were used to walk across activation barriers and record the conformational versatility of the simulated systems. The wave function convergence criteria of 10^{-4} kcal/mol were employed in the self-consistent field algorithm.

The local optimizations of the molecular geometries were conducted through the rational function optimization algorithm. The simultaneously required convergence criteria for a stationary point were set as follows: 0.6 kJ pm^{-1} for the strongest nuclear force, 0.04 kJ nm^{-1} for the RMS nuclear force, 0.9 pm for the largest nuclear displacement, and 0.6 pm for the RMS nuclear displacement. The procedure operated Cartesian coordinates of all atoms.

The chosen reaction coordinates were scanned stepwise in the vicinity of the anticipated transition states. While the reaction coordinate remained rigidly fixed at a certain value, all other degrees of freedom were free to evolve based on the energy gradients. The restrained local geometry optimization was carried out at every value of the reaction coordinate to find the minimum energy. Each reaction coordinate was propagated with a linear step of 1-2 pm. The calculations of the vibrational frequency profiles were conducted for maxima points along the obtained reaction profiles. The frequencies were derived using the conventional rigid rotor approximation. The heights of the maxima relative to the reactant energies represent activation

barriers for the considered chemical transformation. All wave functions related to the reaction profiles were computed by the unrestricted version of the HDFT calculations.

The global minimum energy stationary points were found via the kinetic energy injection method described elsewhere.⁴⁶⁻⁴⁸ One hundred candidate structures per chemical composition were considered. The perturbation kinetic energy was set to 1000 K. The excess energy was injected into systems every 0.1 ps. PM7-MD simulations were used to propagate the nuclear trajectories.

The thermochemical potentials were derived from molecular partition functions in the implicit solvent methanol. The molecules at each state (reactants and products) were treated jointly. The gas phase approximation was not used. For CO₂, it meant that its dissolved state in liquid CH₃OH instead of the gas state was considered. The sequence from Hess's law was applied to get the potentials (Gibbs free energy, enthalpy, entropy) of the chemical reactions. The obtained frequencies were used to compute near- and far-infrared spectra and obtain zero-point energy corrections. It has been added to electronic energies.

The polarizable continuum approach was employed to model the implicit solvation in CH₃OH. The model performs by modifying the Hamiltonian of the system with a solute-solvent coupling term depending on the solute's local electric field.⁵⁷ The effect of solvation was included in all reported properties.

The electronic polarization was described via partial electrostatic charges obtained according to the Merz-Singh-Kollman algorithm.⁵⁸ Throughout the discussion, we use partial atomic charges as quantitative measures of nucleophilicities and electrophilicities of the reactants' interaction centers.

The charge transfer amounts were assessed via the natural bond orbital (NBO) analysis. These processes were characterized by the interaction energies between the localized orbitals. The

energies were computed according to the second-order perturbation theory. Furthermore, the NBO charges on atoms were computed to compare the properties of various interaction sites.

Gaussian09 software was applied to conduct electronic-structure calculations.⁵⁷ VMD 1.9.3⁵⁹ and Gabedit 2.5.2⁶⁰ were used to manipulate the Cartesian and internal coordinates of the simulated systems. The in-home software was used to conduct non-standard simulations and process the numerical results.

3. Experimental methodology

3.1. Materials

Methanol (>99,9% -EMSURE®), sodium chloride ($\geq 99,5\%$, EMSURE®), iodomethane (>99.5%, ALDRICH), diethyl ether (>99.9%, EMSURE®), DMC (>99.5%, ALDRICH), pearl-shaped molecular sieves (3A, ALDRICH), and CO₂ (99,8%, White Martins).

3.2. DMC synthesis

The reactions were conducted in the 120 ml metal reactor with constant magnetic stirring. The temperature was controlled using a thermocouple connected to the temperature controller along with a heating mantle around the reactor. In reactions using the dehydrating agent, the reactor was equipped with an upper metallic compartment (gas phase) filled with molecular sieves. The reactions employed 213 mmol of CH₃OH, and different amounts of NaCl (5.134, 8.556, 11.98, 15.40, 18.82, 25.67, and 34.22 mmol NaCl), and 20 mmol of CH₃I. The reactions were carried out at 40 bar of CO₂ pressure and a temperature of 80°C. Each reaction proceeded 24 hours before the analysis of the products was performed.

All tests were performed in triplicates. The products from the catalytic tests were analyzed by gas chromatography (GC) to determine yield, conversion, and selectivity. The Shimadzu GC-2014 gas chromatograph equipped with an SH-Rtx-5 column was used. The temperature schedule involved a heating ramp of 31°C for 0.5 minutes, 10°C min⁻¹ to 50°C for 1 minute, 20°C min⁻¹ to 100°C for 2 minutes, and 50°C min⁻¹ to 220°C for 2 minutes. The samples were diluted with a 4% (v/v) concentration in ethyl ether. The area of the DMC peak (2.4-2.7 minutes) was used to determine the concentration through the pure DMC calibration curve, following procedures described by Valente, Riedo, and Augusto (2003).⁶¹ The conversions and selectivities were calculated as described elsewhere by Faria and coworkers.^{14,31,62} The pH measurements were carried out using the Digimed DM20 pH meter.

4. Results and discussion

The theoretical part of this work deals with the most energetically demanding stage of the DMC synthesis, which is proton abstraction, i.e., the formation of CH₃O*. Once formed, the metholate radical readily captures CO₂. We provide a comprehensive description of the reactants, transition states, and products involved in this cornerstone process for DMC synthesis. We deliberately used lone cations and ion pairs as separate catalysts to understand how the concentration of the inorganic salt in CH₃OH influences the catalytic performance. The lone ions prevail in dilute solutions, whereas ion pairs are abundant in more concentrated solutions. By comparing both mentioned options, the computer simulations may suggest optimal experimental setups.

4.1. Global minimum search

It was of essential importance to identify the most thermodynamically stable geometry of the intermediate. The $\text{CH}_3\text{OC}(\text{O})\text{O}^-$ anion could be neutralized by H^+ , which leaves the reacting CH_3OH molecule, or the alkali metal cation (Li^+ , Na^+ , K^+). Furthermore, the resulting structure could be solvated in different ways thanks to a few hydrogen bonding sites available. The global minimum search revealed about ten local minimum conformations of every composition. Figure 1 exemplifies the obtained potential energies for the systems containing LiI as a catalyst, whereas other compositions exhibit qualitatively similar behaviors. The versatilities of the obtained structures occur due to the various possible arrangements of H-bonds and the competition of the proton with alkali cations for the location near the oxygen atoms of the hydroxyl groups within the reactants and near the carboxyl group within the products.

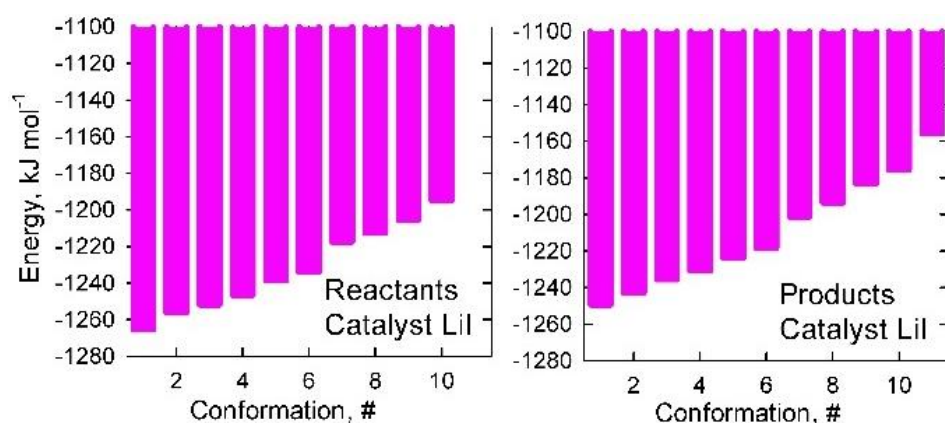


Figure 1. The potential energies of the stationary points in the reactants (3 CH_3OH , 1 CO_2 , and LiI catalyst) and products (1 $\text{CH}_3\text{OC}(\text{O})\text{O}-\text{H}^+$, 2 CH_3OH , and LiI catalyst).

Figure 2 visualizes the selected global-minimum structures containing Li^+ and LiI as catalysts. The alkali cation strongly coordinates a few oxygen atoms of CH_3OH and the emerged carbonate moiety. Another strong attraction takes place between the former hydrogen atom of CH_3OH and the iodide anion. The oxygen and iodine atoms compete for the proton, which is located between them. The two stationary points of similar potential energy stand for the proton covalently attached to iodine and H-bonded to oxygen and vice versa. By definition, iodine does not participate in H-bonding. Yet, its electrostatic attraction to hydrogen is strong. In the systems

without the anion (chloride, iodide), the hydrogen atom is bound to the carbonate moiety in the corresponding global minimum states but may be electrostatically attracted to the solvent (CH_3OH) molecules in higher-energy stationary states.

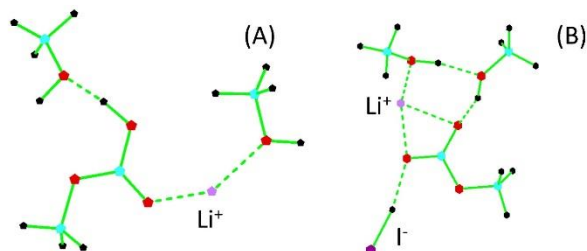


Figure 2. The selected low-energy molecular configurations of the products: (A) catalyst Li^+ and (B) catalyst catalyst LiI . The dashed lines highlight strong electrostatic interactions, including H-bonds.

Figure 3 compares the molecular geometries of the reactant and product compositions, whereas the reaction is catalyzed by the potassium cation. The cation coordinates three CH_3OH molecules and the CO_2 molecule. The hydroxyl groups are polarized thanks to such an electrostatic attraction. In turn, after the reaction, K^+ coordinates only one CH_3OH molecule and the newly formed carbonate group. The remaining solvent molecule diffuses away from the catalyst and forms a strong H-bond, 170 pm long, with the protonated carboxyl group of the product.

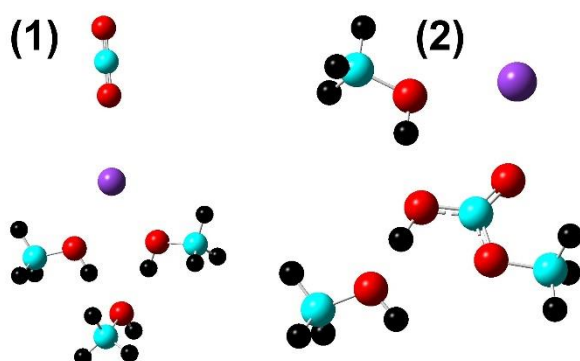


Figure 3. The optimized molecular structures were obtained for (1) reactants and (2) products. The employed catalyst is the potassium cation.

If K^+ is provided as an ion pair, KI , its coordination capability essentially deteriorates (Figure 4). However, the payoff is that the iodide anion coordinates the hydrogen atom of CH_3OH .

As we rationalize below in terms of thermochemistry and activation barriers, this feature plays a paramount role in the simpler deprotonation of the hydroxyl moiety. In the state of products, the location of the catalyst does not change substantially. The reacted system remains to be strongly correlated via the H-bonded network.

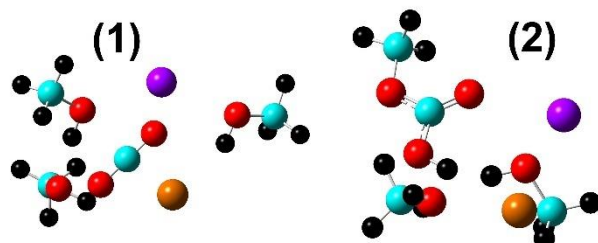


Figure 4. The optimized molecular structures were obtained for (1) reactants and (2) products. The employed catalyst is potassium iodide.

Finding global minimum states for the involved stationary points (reactant, transition state, reaction intermediate, product) is a cornerstone of a trustworthy energetic evaluation. The height of the activation barrier represents an energetic difference between the transition state geometry and reactant geometry. Therefore, choosing a non-global minimum configuration of the reactants proportionally underestimates the applicable activation barrier. The same philosophy should apply to the transition states. While a few transition states may correspond to a given chemical reaction, only the energetically lowest one is followed in real-world syntheses. This lowest activation barrier unequivocally determined the cheapest reaction pathway.

4.2. Binding and cohesion energies

The non-covalent binding energies (Figure 5) within the simulated systems reflect the relative conformational rigidities. On a related note, strong interactions within reactants and products, as well as the solvation energy gain, thermodynamically stabilize the respective system. Consequently, the non-covalent interactions contribute to the thermochemistry of the studied

reactions. The strongest interactions take place within the products upon using the NaCl catalyst, the corresponding potential energy amounting to -798 kJ/mol. In turn, the corresponding reactants exhibit a total non-covalent binding energy of -796 kJ/mol. The difference with other systems comes from the strong hydrogen-chloride H-bonding and strong sodium-oxygen electrostatic attraction. Furthermore, weaker attractions exist between the alkali metal cation and the three remaining polar oxygen atoms located in the proximity. The setups containing the chloride anion appear more correlated with one another as compared to the iodide-containing systems. The present observation suggests that chloride is a somewhat more desirable counterpart of the catalyst. Large negative binding energies in the LiI-catalyzed samples are likely due to the strong coupling between the smallest possible alkali cation with the adjacent nucleophilic centers. Such a feature of lithium is routinely employed in chemical energy sources.⁶³⁻⁶⁴

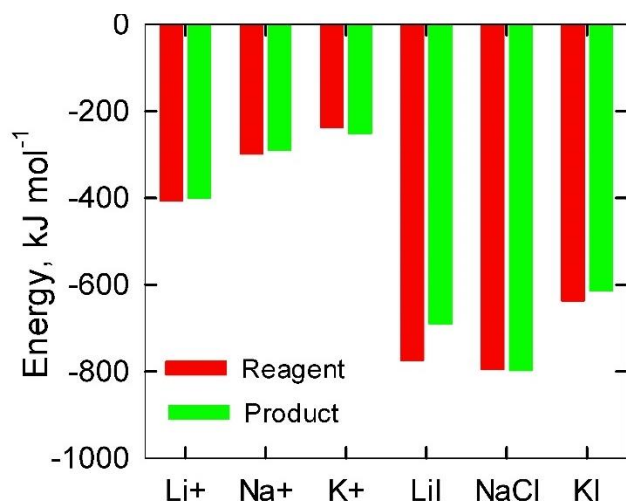


Figure 5. The sums of the non-covalent binding energies in the reactants (red bars) and products (green bars).

The simulated systems were immersed into the implicit solvent, CH₃OH. Table 1 summarizes the molar volumes depending on the molecular compositions of the systems. The CO₂ capture reaction increases the molar volume in all cases except for the KI catalyst. Bulky K⁺I⁻ is known to exist as a rather diffuse ion pair.⁶⁵ The formation of the products fosters a more energetically favorable reorientation of these ions. The latter results in a more compact structure,

which exhibits a somewhat lower molar volume. Note that the reactant configurations may be designated as CO₂ physisorbed in CH₃OH. In turn, the product configurations may be designated as chemisorbed CO₂.

Table 1. The molar volumes of the systems containing physisorbed (reactants) and chemisorbed (products) CO₂.

Process	Li ⁺ , cm ³ /mol	Na ⁺ , cm ³ /mol	K ⁺ , cm ³ /mol	LiI, cm ³ /mol	NaCl, cm ³ /mol	KI, cm ³ /mol
Reactants	88.3	87.5	108	123	145	168
Products	113	99.3	114	153	187	141

The cohesion energies (Figure 6) support the above conclusion regarding the strongest physical interactions in the NaCl-containing system. Furthermore, one notices that the ion pair catalysts exhibit stronger cohesions than the lone cation catalysts. The effect of the anion was not evident without specific calculations. For instance, one could hypothesize that an anion could screen the electrostatic interactions between the cation and the hydroxyl group and, therefore, quench the polarization of the proton originally belonging to the reacting CH₃OH molecule. The simulations revealed that the anions play an essential role in coordinating the hydrogen atom being favorable for deprotonation.

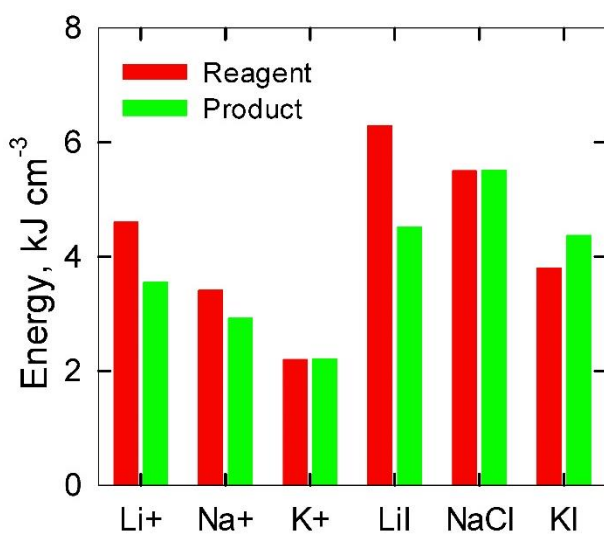


Figure 6. The cohesion energies in the simulated systems represent physisorbed CO₂ (red bars) and chemisorbed CO₂ (green bars).

4.3. Bond lengths, atomic nucleophilicities, and atom-atomic charge transfers

In a strongly correlated system, numerous electron transfers can be identified occurring between higher- and lower-energy orbitals. The most essential charge transfers involve the lone electron pairs of strongly electronegative interaction centers and empty non-bonded orbitals of the more electropositive interaction centers. Such processes decrease the strength of the covalent bonding, if any exists, and increase physical interactions. Specifically, the electron transfers between orbitals are responsible for the strong solvation of small cations in their solutions.

The oxygen atoms of CH₃OH possess lone electron pairs, which interact with the alkali metal cations. The corresponding energies in the case of lithium amount to 96 and 88 kJ/mol. These interactions indicate very strong atom-atomic couplings. Furthermore, Li⁺ interacts with one of the oxygen atoms of CO₂ with an energy of 79 kJ/mol. The presence of the iodine anion substantially quenches the mentioned interactions. The corresponding energies equal 65 kJ/mol with CH₃OH and 11 kJ/mol with CO₂. Noteworthy, no noticeable charge transfer takes place between iodine and hydrogen even though these atoms interact strongly based on the optimized molecular geometries. Their attraction is to a large extent due to Coulombic forces and to a lesser extent due to the overlap of electronic orbitals. For instance, the hydrogen-iodine distance in the KI-catalyzed system amounts to 250 pm.

Table 2 summarizes the strongest physical interactions in the simulated systems. These interactions undermine the stabilities of the covalent bonds and contribute the equivalent portions of potential energy to the stabilization of ion-ionic and ion-molecular couplings. All the interactions take place among the most electronegative sites, oxygen atoms, and three alkali metal cations. The oxygen atoms may belong to any of the CH₃OH, CO₂, and carboxyl moieties. To

exhibit a strong mutual attraction following the charge transfer mechanism, the atoms must be located closer than 300 pm. It means that smaller alkali cations exhibit stronger non-covalent attractions to the oxygen atoms. Compare, a very strong interaction involving CH₃OH and Li⁺ of 96 kJ/mol, whereas the optimized distance between them amounts to 197 pm (Table 3). Interestingly, the interaction of Li⁺ with the protonated carboxyl group is 59 kJ/mol at a distance of 198 pm. The protonation state definitely impacts the amount of charge transfer.

Table 2. The strongest stabilization energies emerging due to partial charge transfers were calculated via the NBO-based analysis. LP designates a lone electron pair. LP* designates an unfilled valence-shell non-bonding orbital.

Pairwise charge transfer	Energy, kJ mol ⁻¹					
	Li ⁺	Na ⁺	K ⁺	LiI	NaCl	KI
Reactants						
LP(O ^{CO2})→LP*(cation)	79	19	26	11	57	52
LP(O ^{CH3OH})→LP*(cation)	96	28	22	65	67	47
Products						
LP(O ^{carboxyl})→LP*(cation)	59	27	17	57	46	51
LP(O ^{CH3OH})→LP*(cation)	52	24	12	59	42	40

An important feature of the CH₃OH-inorganic salt systems is strong ion-molecular coupling. For instance, all cations strongly attract the CO₂ molecule. The charge-transfer-based attraction between K⁺ and CO₂ equals 52 kJ/mol before the reaction. The distance from K⁺ to one of the oxygen atoms of CO₂ is 304 pm. The systems containing both cation and anion generally exhibit large charge transfers as compared to the systems with a cation only. The revealed interactions are commensurate with the high cohesion energies discussed above. We conclude that the alkali cation polarizes not only the CH₃OH but also the CO₂ molecules, which it coordinates.

Table 3. The non-covalent distances, in picometers, between the oxygen atoms and the alkali metal cations in the investigated systems.

Interaction	Li ⁺	Na ⁺	K ⁺	LiI	NaCl	KI
Reactants						

O ^{CO2} - cation	221	278	293	327	253	304
O ^{CH3OH} - cation	197	234	268	192	239	276
Products						
O ^{carboxyl} - cation	198	234	270	202	243	269
O ^{CH3OH} - cation	196	230	267	194	241	271

The analysis of the NBO charges suggests that the cations and anions possess electron densities close to unity. The presence of the anions in the systems somewhat decreases the charges of the cations. The charges in the product configurations are slightly larger than those in the reactant configurations. The NBO charges belonging to the oxygen atoms, which represent electron donors in the considered interactions, appear substantially lower within products. This feature is in line with our expectations because CO₂ acquires an additional electron upon grafting to the methoxy moiety. The obtained electron originally belonged to the hydrogen atom of CH₃OH.

Table 4. The partial atomic charges, in atomic units, on the oxygen and alkali metal ions were recomputed from the localized natural orbitals. The derived charges are in quantitative agreement with the other NBO-based properties.

Species	Li ⁺	Na ⁺	K ⁺	LiI	NaCl	KI
Reactant						
Cation	+0.90	+0.96	+0.96	+0.89	+0.87	+0.86
Anion	—	—	—	-0.91	-0.89	-0.90
O ^{CO2}	-0.54	-0.53	-0.53	-0.52	-0.54	-0.53
O ^{CH3OH}	-0.79	-0.78	-0.78	-0.82	-0.77	-0.75
Product						
Cation	+0.95	+0.97	+0.98	+0.95	+0.91	+0.89
Anion	—	—	—	-0.93	-0.90	-0.88
O ^{carboxyl}	-0.73	-0.70	-0.53	-0.75	-0.70	-0.68
O ^{CH3OH}	-0.73	-0.79	-0.78	-0.80	-0.76	-0.78

The electrostatic partial atomic charges (Figures 7-8) reflect the electrostatic portion of the non-covalent interactions in the simulated systems representing both reactants and products. The charges are obtained via the ab initio-derived electrostatic potential fitting around the system. The electrostatic charges are frequently used to parameterize the Coulombic fractions of the molecular

mechanics Hamiltonians to simulate large atomic ensembles. The charges of the alkali metal cations (Figure 7) are particularly important due to their participation in polarizing the hydroxyl group of CH_3OH . Within products, Li^+ , Na^+ , and K^+ strive to coordinate the newly emerged carbonate moiety as a whole. The carbonate-cation interactions are seen as an important factor that stabilizes the methyl hydrogen carbonate intermediate thermodynamically.

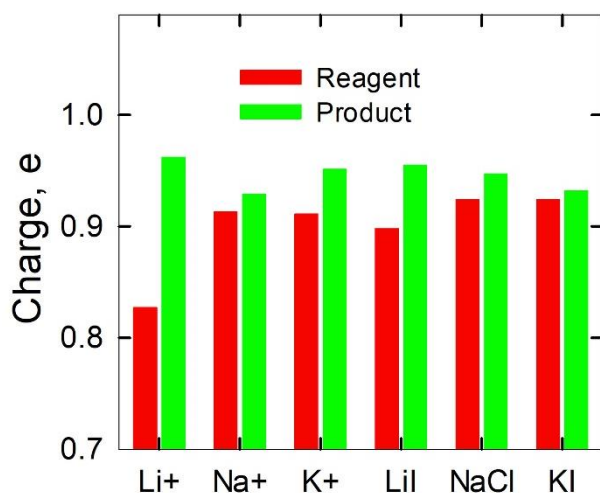


Figure 7. The electrostatic partial charges of the alkali metal cations within the reactants (red bars) and products (green bars) depend on the employed catalyst.

The electrostatic attractions recorded within the products are systematically stronger as compared to those within the reactants. For instance, the charge of Li^+ amounts to $+0.83e$ while coordinating the hydroxyl group of the reactant. In turn, the charge of this cation increases up to $+0.96e$ while it coordinates the protonated carbonate moiety. Furthermore, higher partial electrostatic charges imply stronger attractions with the implicitly and explicitly simulated CH_3OH molecules. These interactions are important product-stabilizing factors that enhance the thermochemistry of the considered reaction stage.

The major non-covalent interactions in the simulated systems take place among the oxygen atoms of CH_3OH , $\text{CH}_3\text{OC}(\text{O})\text{OH}$, and alkali metal cations. The strengths of these stabilizing interactions depend equally on the cation's charge and the oxygen atoms' charges. Figure 8

compares the charges of the oxygen atoms belonging to the hydroxyl groups of the CH₃OH molecules within reactants and products.

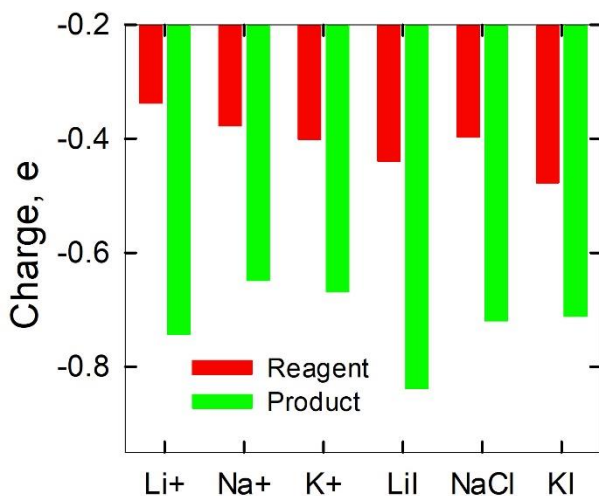


Figure 8. The electrostatic partial charges of the oxygen atom belonging to CO₂ (within reactants, red bars) and the carboxyl moiety (within products, green bars) depend on the employed catalyst.

The surface of the electrostatic potential indicates that the most electron-deficient region includes a cation, whereas the electron-richest regions include an anion and oxygen atoms (Figure 9). The hydroxyl proton maintains an H-bond with the chloride atom. The corresponding distance amounts to 214 pm. The samples catalyzed by LiI and KI do not exhibit pronounced hydrogen-halogen patterns due to a larger atomic radius of iodine. For instance, the H...I distance equals 242 pm (with LiI) and 250 pm (with KI). The hydrogen-anion interactions play a paramount role in determining the thermochemistry of deprotonation as we discuss below. Overall, both the reactant state and the product state are dominated by the Coulombic forces based on the partial atomic charges and electrostatic potential surfaces. The high polarity of the reaction medium is decreased at the termination stage of the DMC synthesis, upon passivating the CH₃OC(O)O⁻ anion with the methyl radical.

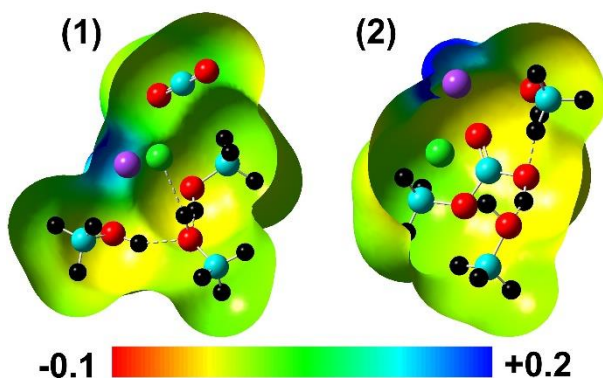


Figure 9. The electron density derived from the total self-consistent-field density (the isovalue equals 4.0×10^{-4} a.u.) mapped with the electrostatic potential for (1) reactants and (2) products. The depicted systems contain NaCl as a catalyst particle. The H-bonds are designated by dashed lines.

The reactant molecules strongly attract to the catalyst before the deprotonation of CH_3OH . Specifically, the halogen atom of the catalyst coordinates the hydrogen atom of the hydroxyl group of CH_3OH . In turn, the alkali atom of the catalyst coordinates the oxygen atom of the hydroxyl group. After the deprotonation, the described coordination patterns are largely retained. Figure 10 depicts localizations of the valence orbitals which are shared by the ions and CH_3OH molecules. The LUMO+1 reveals the partial localization on K^+ . The valence electron formally belonging to the potassium atom is localized on the oxygen atom of CH_3OH . In the LiI-containing system, LUMO (energy of +0.272 eV) is localized on the cation. In the NaCl-containing system, LUMO+4 (energy of +0.318 eV) is localized on the cation. It means that the cations do not have valence electrons in the studied systems. HOMO-2 in the KI-containing sample, HOMO-2 in the LiI sample, and HOMO-3 in the NaCl-containing sample are shared by the iodide/chloride anions and the hydroxyl groups of CH_3OH . These shared electron densities reflect the formation of strong electrostatic interactions. In the case of chloride, the designated attractive interaction qualifies for H-bonding. In all systems, the HOMO-4 levels exhibit similar energies and are shared among all CH_3OH molecules. These molecular orbitals corroborate the CH_3OH - CH_3OH couplings.

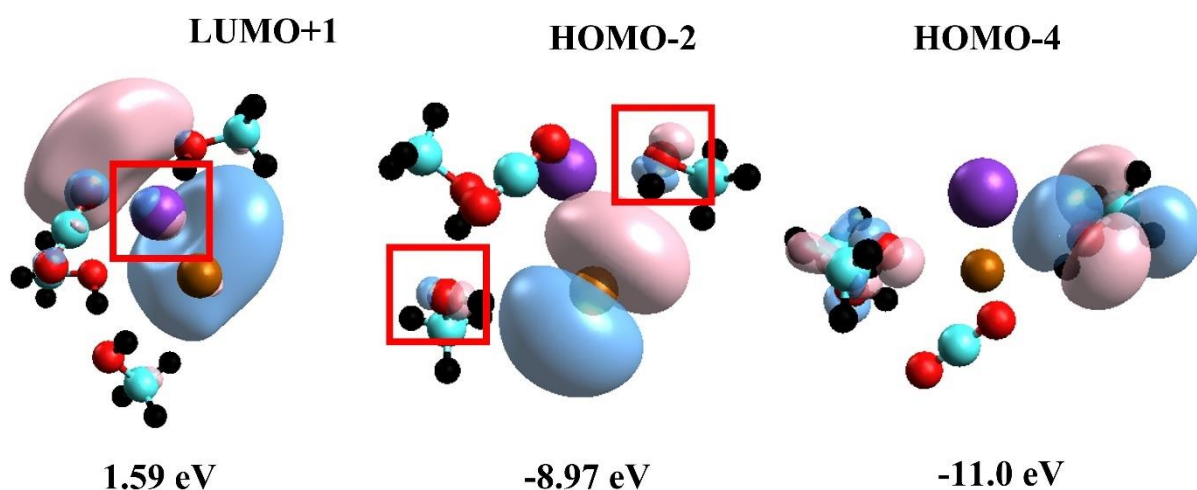


Figure 10. The spatial localization of the selected molecular orbitals in the reactant system containing KI as a catalyst. Potassium is purple, iodide is brown, oxygen is red, carbon is cyan, and hydrogen is black.

4.4. Far- and mid-infrared spectra

Figures 11-13 provide infrared spectra in the systems containing LiI, NaCl, and KI. A direct comparison is made between the reactant and product compositions. The depicted C-O band corresponds to symmetric stretching observed in CH₃OH and the carboxyl moiety. C=O represents symmetric stretching in carboxyl, CO₂ contributes antisymmetric stretching, and O-H groups manifest as symmetric stretchings in CH₃OH and carboxyl. The reactant's signal at 2404 cm⁻¹ corresponds to CO₂ and vanishes in the product state (Figure 11).

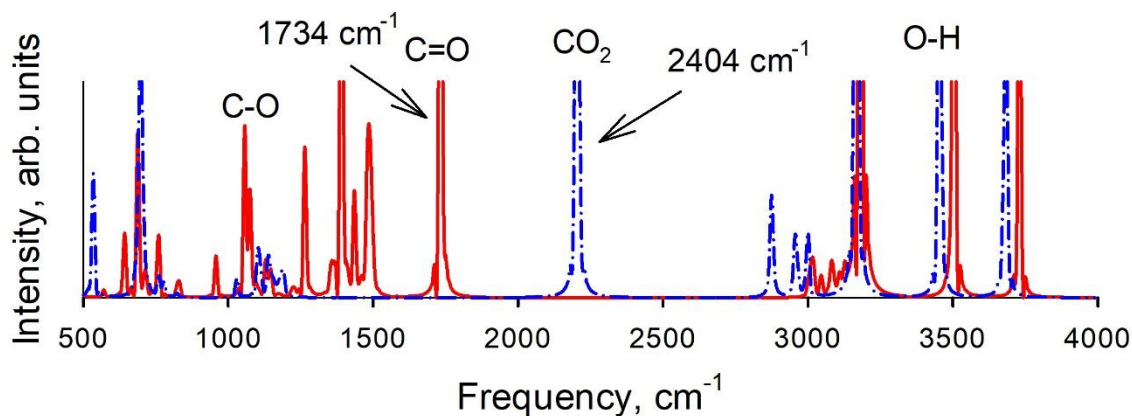


Figure 11. The infrared spectra correspond to the reactant (dashed blue) and product (solid red) of the reaction catalyzed by LiI.

The C-O band corresponds to symmetric stretching in CH₃OH and carboxyl. The signal at 1774 cm⁻¹ is symmetric stretching in carboxyl, the C=O double bond. The asymmetric stretching taking place in CO₂ shifts by 2 cm⁻¹ rightward, as compared to the LiI-containing system. The very strong 162 pm-long hydrogen-oxygen H-bond stretches symmetrically at 2912 cm⁻¹. It unites the emerged carbonate moiety with the neighboring hydroxyl group of the solvent. Additionally, vibrational spectroscopy reveals the formation of the O-H...Cl H-bond, 213 pm-long, thanks to a signal at 3451 cm⁻¹. This bond exists both within reactants and products. Its length in the product state is 1 pm smaller than in the reactant state, whereas the corresponding frequency in the product state is 3412 cm⁻¹ (Figure 12).

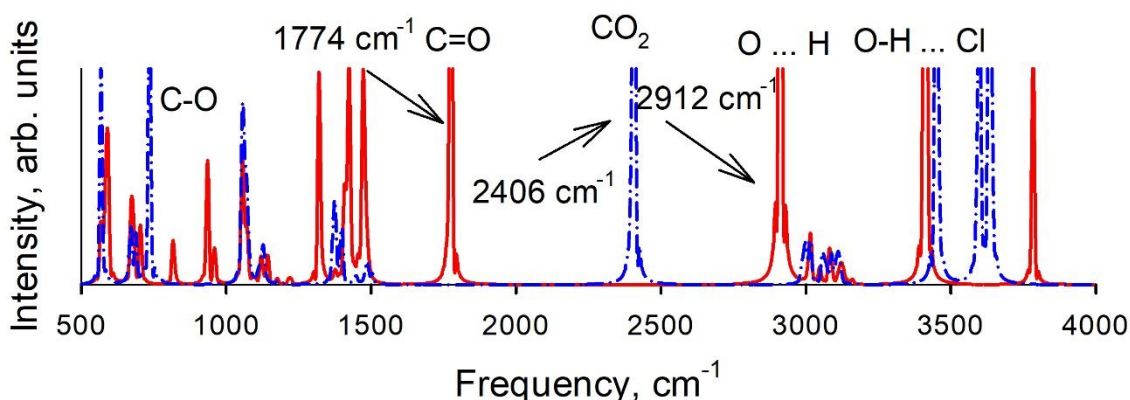


Figure 12. The infrared spectra correspond to the reactant (dashed blue) and product (solid red) of the reaction catalyzed by NaCl.

The KI-catalyzed system exhibits the symmetric C=O vibration within the carboxyl group at 1783 cm⁻¹, the antisymmetric stretching of the carbon-oxygen double covalent bond in CO₂, and the O-H symmetric stretching band in CH₃OH and -COOH. The key observed frequencies are reasonably similar in all catalyzed samples. This feature suggests the principal similarity of the studied reactions upon the application of the inorganic salts to activate CH₃OH (Figure 13).

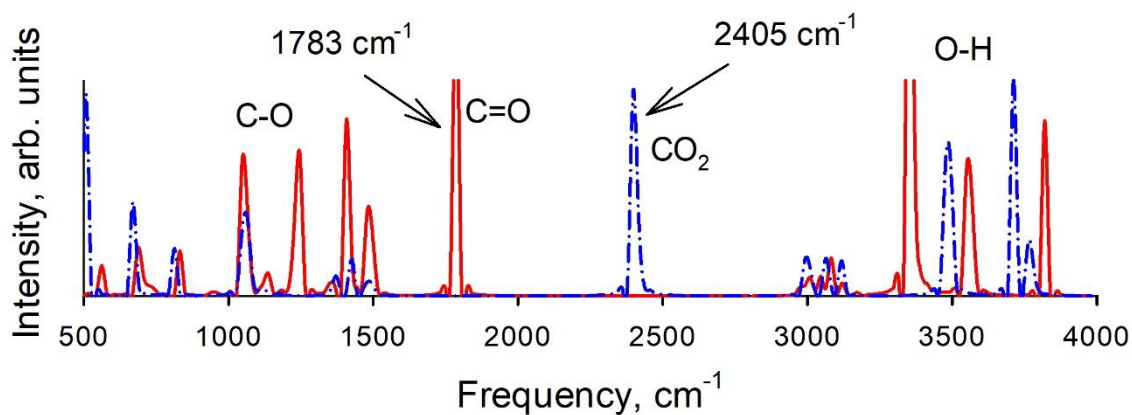


Figure 13. The infrared spectra correspond to the reactant (dashed blue) and product (solid red) of the reaction catalyzed by KI.

4.5. Thermochemical potentials

The thermochemical potentials for the deprotonation of CH_3OH and subsequent carboxylation of CH_3O^* are provided in Tables 5-7. The reactions are enthalpically favored and entropically forbidden. The increase in temperature leads to a slight deterioration of the Gibbs free energy. Hence, the yields of the DMC synthesis are expected to be poorer at elevated temperatures. In the meantime, the elevated temperatures are important measures to overcome the activation barriers. The effects of the ion pairs as catalysts at this stage compared to the lone cations are uncertain. For instance, the performance of NaCl , +10.6 kJ/mol at standard conditions, is better than that of Na^+ , +23.7 kJ/mol. However, the relations are opposite in the cases of the LiI and KI catalysts. In general, the obtained free energies are close to zero suggesting that the discussed stage is a yield-limiting one.

Table 5. The Gibbs free energies of the $\text{CH}_3\text{OH} + \text{CO}_2 = \text{CH}_3\text{OC}(\text{O})\text{OH}$ reaction at a set of temperatures and ambient pressure for the various employed catalysts.

System	Temperature, K					
	250	280	298.15	330	360	390
Li^+	-2.57	-1.01	-0.058	+1.62	+3.21	+4.80
LiI	+23.9	+25.4	+26.4	+28.2	+29.9	+31.7
Na^+	+21.3	+22.8	+23.7	+25.4	+27.0	+28.7

NaCl	+8.24	+9.72	+10.6	+12.3	+13.9	+15.5
K ⁺	-0.205	+0.764	+1.35	+2.36	+3.31	+4.25
KI	+23.6	+26.5	+28.2	+31.4	+34.4	+37.6

Note that the catalysts should not influence the thermochemistry of the aggregate DMC synthesis. However, they do impact the energetics of the individual reaction stages due to the somewhat different coordinations of the reactant and product species. The locations of the catalyst particles during the reaction may boost or deteriorate the feasibility of certain elementary processes. The temporarily acquired difference in potential energy is returned upon the final stage of the DMC synthesis, which is $\text{CH}_3\text{OC}(\text{O})\text{OH} + \text{CH}_3\text{I} = \text{CH}_3\text{OC}(\text{O})\text{OCH}_3 + \text{HI}$. The catalyst ions reorient and alter their potential energies in response to the formation of new molecules. Yet, the effects of the catalysts on the individual stages of the synthesis have a physical sense and contribute to the feasibility of the local chemical transformations.

Table 6. The enthalpies of the $\text{CH}_3\text{OH} + \text{CO}_2 = \text{CH}_3\text{OC}(\text{O})\text{OH}$ reaction at a set of temperatures and ambient pressure for the various employed catalysts.

System	Temperature, K					
	250	280	298.15	330	360	390
Li ⁺	-15.5	-15.6	-15.7	-15.8	-15.9	-15.9
LiI	+11.3	+10.5	+10.1	+9.44	+8.85	+8.29
Na ⁺	+9.08	+8.50	+8.16	+7.60	+7.09	+6.61
NaCl	-3.84	-4.27	-4.52	-4.93	-5.27	-5.59
K ⁺	-8.27	-8.25	-8.22	-8.14	-8.02	-7.88
KI	+0.646	-0.333	-0.903	-1.87	-2.74	-3.57

The Li-ion-containing system exhibits the most favorable enthalpy and Gibbs free energy. This phenomenon might have been predicted based on the strong electrostatic attraction of this cation to the polar reactants and products. One should keep in mind that the height of the activation barrier discussed below represents a more important descriptor of the reaction. The NaCl-

containing system also displays a competitive thermochemistry. The role of the chloride anion strongly coupling with the hydrogen atom of CH₃OH must be highlighted.

Table 7. The isobaric heat capacities, standard entropies, and entropic factors, $-T\Delta S$, of the CH₃OH+CO₂=CH₃OC(O)OH reaction for the various employed catalysts.

System	$C_p, \text{J mol}^{-1} \text{K}^{-1}$	$\Delta S, \text{J mol}^{-1} \text{K}^{-1}$	$-T\Delta S, \text{kJ mol}^{-1}$
Li ⁺	-3.93	-52.5	+15.7
LiI	-23.7	-54.7	+16.3
Na ⁺	-19.1	-52.2	+15.6
NaCl	-14.2	-50.8	+15.2
K ⁺	+0.982	-32.1	+9.57
KI	-32.2	-97.7	+29.1

4.6. Transition states and reaction energy profiles

We assume that the deprotonation of CH₃OH and the carboxylation of the emerged CH₃O* species take place simultaneously. Figure 14 demonstrates a starting geometry that was used to obtain the second-order saddle point. The conventional covalent hydrogen-oxygen and oxygen-carbon bonds, ~110 pm long and 140 pm long, were stretched forcibly by roughly ~15-20%. The corresponding redundant internal coordinates were added to the Z-matrix. The geometry optimization algorithm was employed to locate the maximum points along the defined degrees of freedom by moving uphill in terms of energy. However, we were unable to find the imaginary vibrational frequency or two frequencies corresponding to the deprotonation and carboxylation within the explored reason. The alternative routes of the reaction were also attempted as follows. First, the proton transfer was attempted to the adjacent CH₃OH molecule. This route was suggested by the initial optimized geometry of the reactant molecular configuration, in which the hydroxyl group of each CH₃OH forms H-bonds with the adjacent solvent molecules. Recall that we represented three CH₃OH molecules explicitly to consider the local reactant structure to the maximum possible extent. Second, the proton transfer was attempted to the chloride/iodide anion. Nonetheless, the movement along this reaction coordinate also did not reveal an imaginary

frequency. The subsequent stepwise scanning of both coordinates revealed that the energy smoothly rises upon deprotonation. This observation suggested the absence of the hunted transition state in the direct vicinity of CH_3OH .

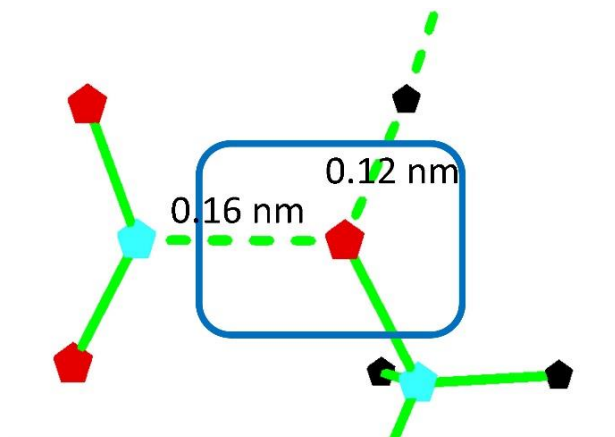


Figure 14. The geometry of the second-order saddle point candidate. The depicted molecular configuration was also used as a starting point to stepwise scan the two reaction coordinates (see dashed lines) by incrementing the bond length by 2 pm. The surrounding CH_3OH solvent molecules were removed for clarity.

To shed light on the energetic alterations at the beginning of the reaction, we compared the thermodynamic stabilities of the proton solvated by liquid CH_3OH to the proton joining the catalyst and also remaining solvated. The energy profile was recorded for the direct proton transfer from the CH_3OH molecule to the HCl molecule. It was found that Cl^- appears an essentially more preferable destination for the proton. The potential energy difference between the considered states amounts to 60 kJ/mol. Nonetheless, both possible locations of the proton constitute stationary points, that is, they can exist for a certain amount of time. The proton exchange process exhibits an activation barrier of 15 kJ/mol. Such barriers are low and are comparable with the steric (physical) obstacles in liquid phases. They are easily overcome at room and elevated temperatures. We hereby conclude that the anion of the catalyst is a dominant host for the proton of CH_3OH . Therefore, the halogen-involving reaction pathway must be further explored, whereas the CH_3OH -involving reaction pathway may be neglected.

For comprehensiveness of the reaction description, we also investigated the simplified related patterns, one by one. Figures 15-16 provide the reaction energy profiles for the hydrogen abstraction in pure CH_3OH and in the presence of the catalysts. The presence of CO_2 in the solution was at this stage deliberately neglected. All catalysts exhibit positive effects on the deprotonation by polarizing the hydroxyl moiety's covalent bond. In the dilute solutions, the strongest positive impact was recorded with Li^+ , whereas the effects of sodium and potassium were similar. In the cases of the more concentrated solutions, the strongest decrease in the energy cost of the proton abstraction reaction was recorded in the NaCl -containing system.

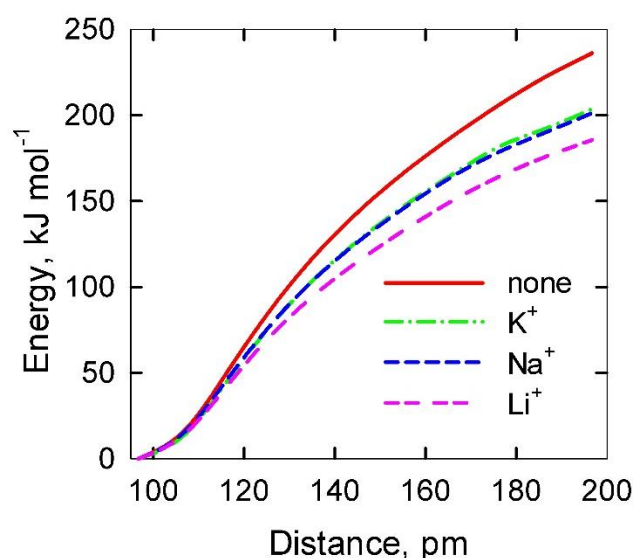


Figure 15. The energy cost of the CH_3OH molecule deprotonation in neat liquid and the presence of the Li^+ , Na^+ , and K^+ catalysts. CO_2 does not participate in the hereby studied deprotonation. See the legend for the designation of lines.

The difference in performance of NaCl relative to LiI and KI can be rationalized through H-bonding between the chloride anion and the hydroxyl hydrogen atom. This strong attraction weakens the bond and simplifies the emergence of the CH_3O^* moiety, which subsequently binds CO_2 without an activation barrier. In turn, the electrostatic attraction occurring between iodine and hydrogen is less thermodynamically favorable. According to conventional IUPAC-recommended

terminology, only smaller halogen atoms – fluorine and chloride – form H-bonds, whereas larger halogens – bromine and iodine – do not.

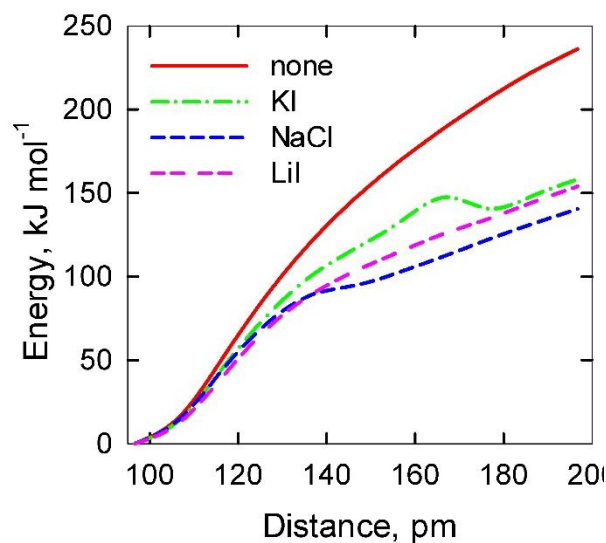


Figure 16. The energy cost of the CH_3OH molecule deprotonation in neat liquid and the presence of the LiI, NaCl, and KI catalysts. CO_2 does not participate in the hereby studied deprotonation. See the legend for the designation of lines.

While the inorganic ionic catalysts exhibit definitely positive effects on the proton abstraction, the corresponding energy costs remain high. Furthermore, the penalizing energies smoothly rise without drawing an energy maximum, i.e., activation barriers. Neither the emerging hydrogen halogenides nor CH_3OH solvating the proton is enough thermodynamically favorable to give rise to stationary points. The effects of the alkali metal cations coordinating the CH_3O^* radicals are also not strong enough. The reaction intermediates must be stationary points as a rule. Furthermore, it is clear that the implied activation barriers – to be found – are not commensurate with the experimentally determined yields of DMC. The hereby reported results suggest that CO_2 must play an important role from the stage of deprotonation. Its effect cannot be ignored upon the proton abstraction. Figure 17 provides the reaction energy profiles for the carboxylation stage. This instance of simulation deliberately neglects the proton of CH_3OH to separate the energy effects along the different reaction coordinates. The carboxylation partially compensates for the

proton detachment penalty. For instance, the stage proceeds without a barrier and brings over -70 kJ/mol to the system. The effect of an alkali metal coordinating CH_3O^* is not essential.

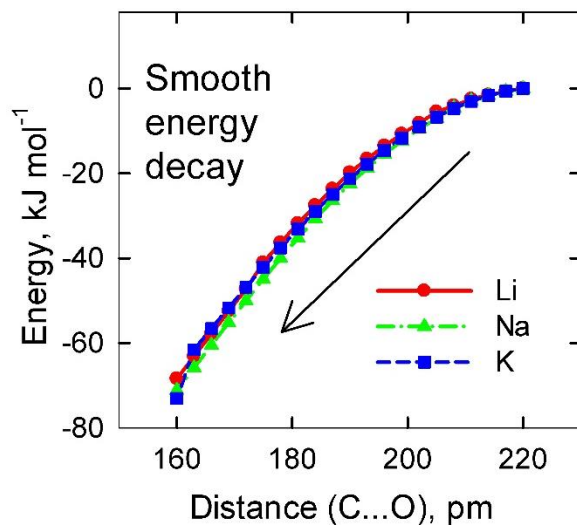


Figure 17. The total electronic energy gains upon CO_2 attachment to deprotonated CH_3OH (carboxylation) at various oxygen-hydrogen distances (degrees of deprotonation) in CH_3OH . See the legend for the designation of lines.

The joint analysis of the deprotonation and carboxylation returns one to the model, according to which CO_2 must form the covalent bond with CH_3OH simultaneously with its deprotonation. Since there is no transition state in the vicinity of CH_3OH , it must be located in a different region of the configurational space.

At this stage of research, we changed the reaction coordinates to $\text{C-O}\dots\text{H}$ and $\text{H}\dots\text{O-C-O}$, wherein the former designates the distance within the hydroxyl group and the latter designates the distance from the hydroxyl hydrogen atom to the oxygen atom of CO_2 (emerging carboxyl group). The $\text{O}\dots\text{C}$ reaction coordinate corresponding to the CO_2 attachment to CH_3OH , which was seen as a natural choice previously, was abandoned. It was possible to obtain a set of first-order saddle points employing such a setup (Table 8). The identified transition states feature high imaginary frequencies, which correspond to antisymmetric radial stretchings. The similar imaginary frequencies reflect similar shapes of the potential energy landscapes in these regions of the

potential energy landscapes. The highlighted similarities have been confirmed by the key interatomic distances, such as O...C, H...O-C-O, and H...O-C, see Table 8.

Table 8. The parameters characterizing the high-energy transition states pertaining to hydrogen transfer from the hydroxyl group of CH₃OH to the carboxyl group of methyl hydrogen carbonate.

Catalyst	Barrier height, kJ/mol	O...C distance, pm	H...O-C-O distance, pm	H...O-C distance, pm	Imaginary frequency, cm ⁻¹
Li ⁺	186.8	150	134	119	1653i
LiI	186.6	146	136	118	1667i
Na ⁺	172.8	147	134	120	1678i
NaCl	188.3	146	135	119	1666i
K ⁺	171.5	148	134	120	1678i
KI	178.0	150	135	119	1668i

Figure 18 visualizes the geometries of the two stationary points, CH₃OH + CO₂ and CH₃OC(O)OH, and the transition state connecting them. Table 8 summarizes all the applicable descriptors. Furthermore, we highlight the locations of the catalyst ions relative to the reactant and product species as well as the activated complex of the reaction. In all considered cases, the NaCl catalyst rigorously coordinates the polarized hydrogen and oxygen atoms. While the coordination in the reactant state activates the deprotonation reaction, the coordination in the product state thermodynamically stabilizes the carboxylated species. These molecular configurations confirm the importance of the inorganic salt catalysts for the newly found reaction mechanism.

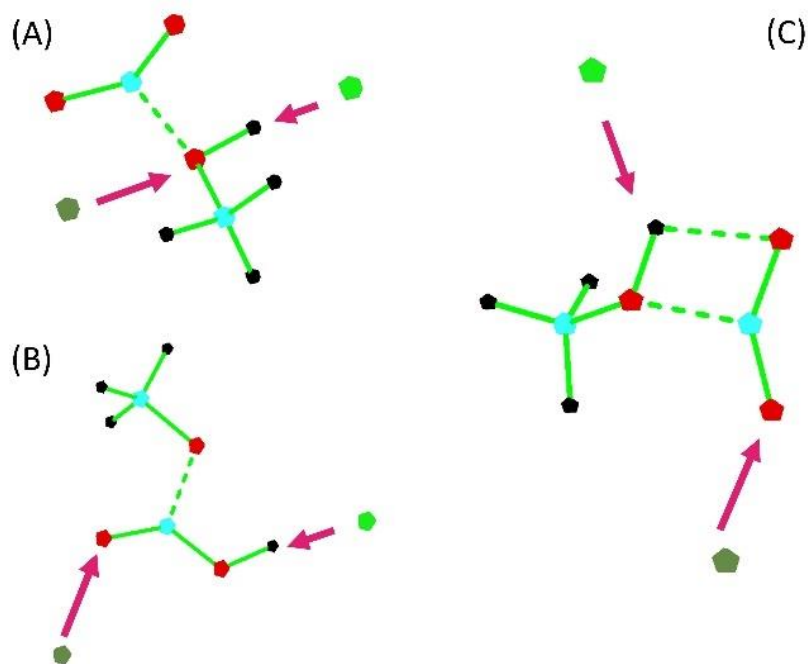


Figure 18. The geometries of the stationary points depict the mutual locations of the reactant/products and catalyst particles at the carbon-oxygen bond length of 160 pm. (A) Beginning of proton transfer. (B) End of proton transfer. (C) Transition state. The lithium atom is dark green and the chlorine atom is light green.

The identified transition states exhibit noteworthy geometries, which point to significant strains in the molecular structures. These structural peculiarities are driven by the geometries of the starting and finishing stationary states since the hydrogen atom must leave CH_3OH at the same time when CO_2 acquires its electron and transforms into the carboxyl group. For instance, the intramolecular strain is reflected by an unusually small $\text{O}\dots\text{C}$ distance of 146-150 pm. If the atoms were not constrained by the emerging geometry of methyl hydrogen carbonate, the $\text{O}\dots\text{C}$ distance must have been about 180 pm. In turn, the $\text{H}\dots\text{O}$ breaking bond is restrained less severely, the distances being 118-120 pm. The $\text{H}\dots\text{O}-\text{C}-\text{O}$ distances look most relaxed, 134-136 pm. They correspond to roughly 35% elongation of the forming oxygen-hydrogen covalent bond to finish the building of methyl hydrogen carbonate. The intramolecular strains within the transition state geometries are reflected by the heights of the activation barriers (Table 8). Recall that the barrier height represents an electronic energy difference between the transition state and the reactant state supplemented by the difference in the associated zero-point energies. The identified barriers

appear surprisingly high versus our a priori expectations. Based on conventional chemical wisdom coupled with the above-reported ab initio analysis and experimentally obtained DMC yields, see below, we would presently anticipate the major barriers to be lower than 100 kJ/mol.

The activation barriers range from 186.8 kJ/mol in the case of the lone lithium ion to 171.5 kJ/mol in the case of one potassium ion. They are comparable with the energy costs for proton abstraction reported above. Lithium may exhibit a slightly poorer performance because it strongly binds to the carboxyl group and hinders its protonation. Still, the difference between Li^+ and K^+ is not commensurate with the difference between expected and located activation barriers. Furthermore, we deliberately compared the catalysis by the cation and anion taken together to the catalysis of the cation alone. Lone cations exist in dilute solutions. As the cations in such solutions can catalyze the reaction in the absence of the anion, their effects must be isolated and evaluated properly. Ion pairs exist in relatively concentrated solutions. In such a case, both the cation and the anion coordinate the same CH_3OH molecule. The solutions of high concentrations may contain larger ionic aggregates and they are probably adverse to the catalytic performance.

Thus far, we found that CO_2 plays a major role in the determination of the transition state upon the formation of methyl hydrogen carbonate. However, the located transition states have unexpectedly high potential energies due to their strained geometries. While the discussed transition states are formally correct and connect the reactants with the products, they are not likely to populate the lowest-energy reaction pathway. If these barriers were the only ones pertaining to the DMC synthesis reactions, the yield of the reaction must have been way smaller than we know from the experiments. Therefore, the search throughout the potential energy surface for the possible transition states must be continued to find lower-energy barriers. Note that the minimum-energy reaction mechanism is preferentially followed, whereas alternative higher-energy reaction pathways may stay unattended despite formally existing. The goal of the research is to unravel the possibly energy-cheapest route.

Figure 19 demonstrates the newly proposed reaction pathway. First, CO_2 collides with the hydroxyl group of CH_3OH . The reaction coordinate used to control this stage is $\text{C-O}\dots\text{C}(\text{O}_2)$, whose value is stepwise reduced by 1 pm. This phenomenon is associated with a relatively sharp potential energy increase, by over 20 kJ/mol depending on the catalyst, in the reacting system. In response to the emergence of the carbon (CO_2)-oxygen (CH_3OH) bond, the hydrogen atom of the hydroxyl group elongates its bond with the oxygen atom and forms a stronger H-bond with a halogen anion. After the carboxylation finishes, we rigidly freeze the $\text{C-O}\dots\text{C}(\text{O}_2)$ reaction coordinate and activate the $\text{H}\dots\text{O-C}$ coordinate. The latter increases stepwise by 1 pm until the transition state is located. The exploration of the energy profile terminates after the carboxyl group of methyl hydrogen carbonate gets protonated. See negative potential energies close to the reaction coordinate value of unity.

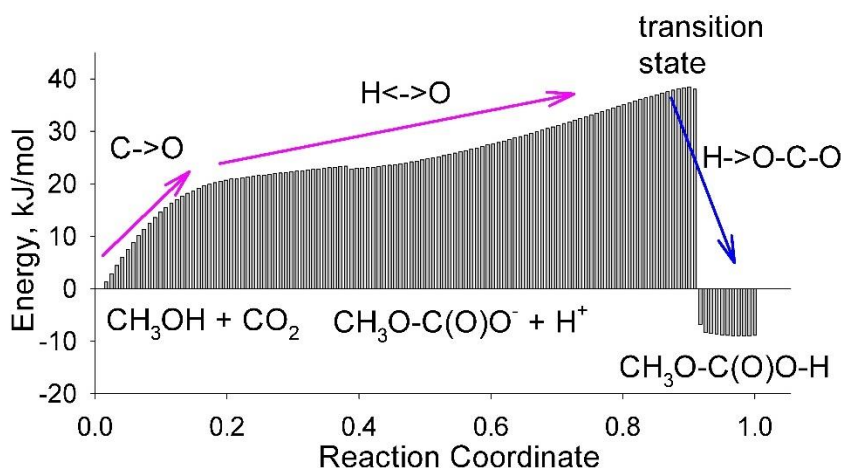


Figure 19. The schematic representation of the minimum-energy reaction path exploration. The depicted reaction coordinate includes a few independent degrees of freedom. The energetic data describing simultaneous deprotonation and carboxylation catalyzed by NaCl was used as a basis for the plot. Note that the plotted numbers are illustrative. The high-quality energies are given in Table 9.

The parameters characterizing the novel set of transition states are given in Table 9. These transition states are substantially different from the previously found set. For instance, the $\text{H}\dots\text{O-C}$ distances amount to 197-216 pm as opposed to 118-120 pm in the strained transition state geometries. It is noteworthy that the transition states are located relatively far from the CH_3OH

molecule. Based on the interatomic distances, they cannot correspond to the hydroxyl group breakage. Indeed, the investigation of the imaginary vibrational frequencies reveals their association with the rocking vibrations. Note that the proton is covalently bound to the halogen anion rather than to the CH₃OH molecule in these transition states. Consequently, the discovered rocking vibrations involve the halogen anion, the hydrogen ion, and the carboxyl moiety.

Table 9. The parameters characterizing the minimum energy transition states pertaining to hydrogen transfer from the hydroxyl group of CH₃OH to the carboxyl group of methyl hydrogen carbonate.

Catalyst	Barrier height, kJ/mol	H...O-C distance, pm	H...O-C-O distance, pm	Imaginary frequency, cm ⁻¹
LiI	98	216	189	267i
KI	101	204	232	134i
NaCl	38	197	210	150i
LiCl	36	201	258	219i

The entire revealed reaction mechanism is summarized in Figure 20. The first three frames were recorded upon the O...C(O₂) reaction coordinate steering, whereas the last three frames were recorded upon pulling hydrogen away from CH₃OH. The images highlight the role of the anion in transferring the hydrogen atom from CH₃OH to CH₃OC(O)O⁻. The formation of the hydrogen-halogen covalent bond greatly decreases the overall energy of the reacting system. Keep in mind that the first stage of steering finished exactly at the value of the O...C(O₂) reaction coordinate equivalent to the previously identified oxygen-carbon bond length in the methyl hydrogen carbonate. The second stage of steering finished ten steps, i.e., 10 pm after the target molecule formed. As a result, the entire path of the studied reaction was recorded. By definition, this must be the minimum-energy reaction pathway assuming that the chosen reaction coordinates reflect real-world chemistry.

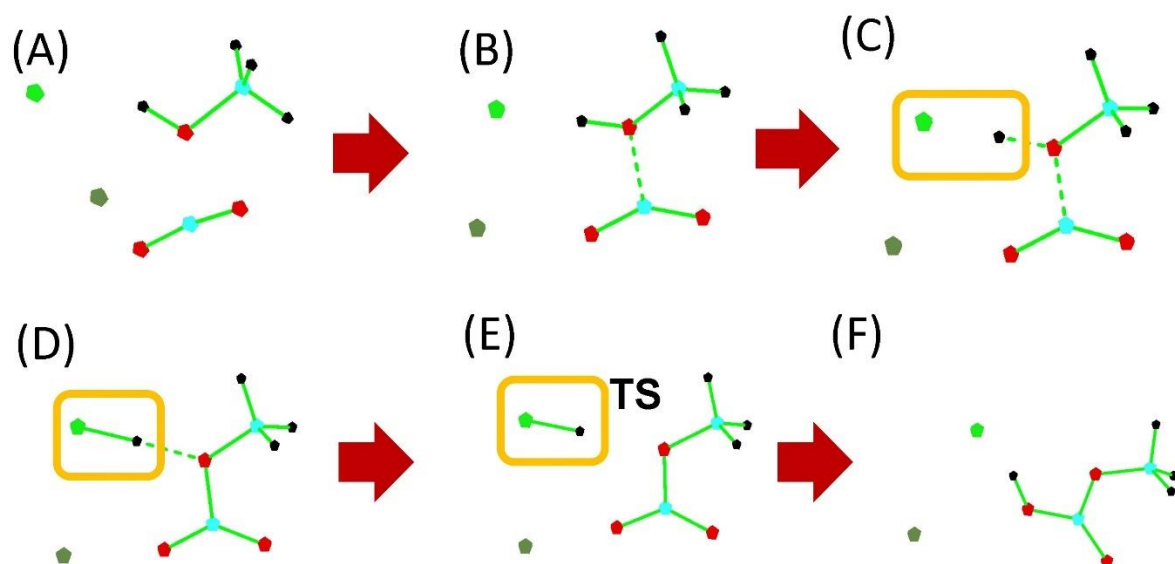


Figure 20. The lowest-energy proton abstraction and simultaneous carboxylation pathway for CH_3OH . (A) CO_2 approaches CH_3OH upon thermal motion. A cation coordinates hydroxyl oxygen and CO_2 oxygen and an anion coordinates hydroxyl hydrogen. (B) CO_2 is forming a covalent bond with oxygen. The $\text{C}\dots\text{O}$ distance amounts to 170 pm. A cation moves farther from the hydroxyl oxygen. (C) The proton detaches from CH_3OH . The $\text{C}\dots\text{O}$ emerging covalent bond length is 155 pm. The $\text{O}\dots\text{H}$ breaking covalent bond length is 115 pm. (D) The breakage of the O-H covalent bond (at the internuclear separation of 158 pm) and the formation of the H-Cl covalent bond (length of 135 pm). (E) The diffusion of the hydrogen chloride molecule toward the carboxyl group. The H-Cl bond length amounts to 131 pm. (F) The protonation of the carboxyl group. The O-H bond length equals 100 pm. The $\text{H}\dots\text{Cl}$ H-bond immediate length equals 153 pm.

Much lower activation energy barriers were hereby located. Relative to the direct scans of the proposed integral reaction coordinate, the nuclei-electronic energies of the stationary points were corrected by the zero-point energies (Table 7). We found that the identity of the anion is greatly important for the catalysis. Compare the barrier of 101 kJ/mol in the system catalyzed by KI to the barrier of 38 kJ/mol catalyzed by NaCl . To confirm the outstanding role of the anion, we computed the activation barrier for LiCl and obtained 36 kJ/mol, which appeared much closer to NaCl than to LiI . The impact of the anion can be rationalized if we consider its role as a carrier of a proton between the two stationary points.

The role of the catalytic action of the cation can also be recorded. For instance, both LiCl and LiI are more successful compared to NaCl and KI . However, the energetic differences are modest. Smaller cations exhibit somewhat better performances thanks to their stronger

coordination of the CH_3O^* radical and saturating $\text{CH}_3\text{OC}(\text{O})\text{O}^-$, which represents a part of the activated complex. All the new transition states are much lower in energy, both before and after zero-point energy supplementation than the strained transition states, even though these new complexes are farther from the state of the reactants, in terms of molecular geometry.

Since more trustworthy activated complexes were unraveled and their location along the low-energy reaction pathway was rationalized, we terminated the search at this point. Due to a high energy difference, we expect that only a low-energy line of transition states makes practical sense. The activation barriers of 36-38 kJ/mol are unprecedentedly small compared to all previous findings in this field. Unfortunately, the yield of DMC is limited by poor thermochemistry, which a low activation barrier cannot compensate for. Yet, faster reaction rates should be expected and the reaction conditions can be made less aggressive. According to the previously published thermochemistry and related energetics,^{14,31-33} the pressure elevations somewhat shift the equilibrium of DMC synthesis rightward.

5. The experimental synthesis of DMC out of CH_3OH using the NaCl catalyst

The goal of the performed experiments is to corroborate the above-discussed theoretical predictions. The NaCl salt was evaluated as a catalyst herein because of the excellent simulation results and the obvious cheapness of this catalyst. The syntheses were carried out under so-called mild conditions. We always look for milder experimental conditions to be more feasible in a real-world industrial process. Milder experimental conditions are less energy-demanding, besides the security and price of the involved equipment. Table 10 summarizes the descriptors of the DMC syntheses by varying the content of the catalyst and temperature in the presence and absence of the dehydrating molecular sieves.

Table 10. The yields and selectivities of the DMC syntheses were obtained by employing various experimental setups. The catalyst is NaCl. The molecular sieves were used for the dehydration of the reaction media. The provided pH values correspond to the end of the reaction.

#	Sieve (g)	Catalyst (mmol)	T (°C)	Selectivity (%)	Yield (%)	pH
1	2.0	5.13	80	100	0.5	3.90±0.03
2	2.0	8.55	80	100	11.42	3.67±0.02
3	2.0	11.98	80	100	16.24	3.60±0.02
4	2.0	15.40	80	100	17.03	3.65±0.02
5	2.0	18.82	80	100	18.69	3.51±0.02
6	2.0	25.67	80	100	16.34	3.40±0.02
7	2.0	34.22	80	100	15.87	3.44±0.02
8	2.0	11.98	90	100	16.89	3.57±0.03
9	2.0	11.98	100	100	16.08	3.52±0.02
10	0.0	11.98	80	100	14.98	3.65±0.02
11	0.0	18.82	80	100	16.78	3.53±0.03

The universal parameters: pressure (40 bar); n (CH₃OH) = 213 mmol; n (promoter, CH₃I) = 20 mmol; reaction duration, t = 24 hours.

The best yields of DMC range from about 17 to about 19%. The usage of extreme CO₂ pressures would somewhat increase these values. This is because a higher pressure compensates for an entropic penalty for the binding of the gaseous reactant.^{14,31-33} However, the energetic cost of such an improvement would unlikely be sustainable upon technological implementation. The role of the dehydrating agent is marginal (compare entries 3 and 10 to entries 5 and 11) unlike in any competitor technologies. It means that the major route of the DMC synthesis does not produce water. The achievement is unique and greatly simplifies the laboratory setup.

At very small contents of NaCl, the yield of the product is marginal at 80°C and 40 bar. We herein assume that the reaction proceeds too slowly and does not finish in 24 hours. In heterogeneous catalysis, the concentration of the provided catalyst is a cornerstone parameter. The larger quantities of the NaCl catalyst result in higher yields (see entries 1 to 5). However, with the further increase of the catalyst content, the DMC yields deteriorate (see entries 6 and 7). Higher ionic concentrations lead to the formation of large ionic clusters, which lose their catalytic activity.

The effect of the higher temperature of the reactions, 90-100°C, was additionally considered. Since the synthesis of DMC is limited by the high activation barrier (proton abstraction from

CH₃OH), larger kinetic energies of the reactants may boost the conversion. At the same time, the increase in temperature makes the thermochemistry of the DMC production reaction less favorable, as we reported previously. Therefore, there are two competing factors in action. The reactions conducted at 90°C and 100°C (entries 8 and 9) had little effect on the DMC yield, as compared to entry 3.

The hereby achieved DMC yield is seemingly close to the theoretical limit, which emerges due to the relative thermodynamic stabilities of CH₃OH, CO₂, and DMC.^{14,31-33} This opinion is empirically confirmed and theoretically rationalized by the recent results of Faria and coworkers.⁶² Therein, 0.7g of the CH₃OK catalyst was applied in the presence of a molecular sieve under the pressure of 40 bar and the temperature of 80°C. The DMC yield of 17.2% was obtained after 24 hours. The same conditions applied in the present work to NaCl provided a fairly similar DMC yield of 16.24%. NaCl is a much more affordable catalyst than CH₃OK. Among other properties, CH₃OK represents quite an unstable compound.

The hypothesis used in the above-reported computer simulations was that the proton that leaves CH₃OH eventually joins one of the available anions, either iodide originating from iodomethane or iodide/chloride originating from the catalyst. At low proton contents, these subproducts must exist in a dissociated state and do not impact the catalytic activity. To verify the identity of the simulated and in-vitro reactions, pH was measured experimentally in the product state (Figure 21). The results indeed indicate an acidic reaction of the media after the reaction. Note that the neutral reaction in CH₃OH corresponds to a pH value of 8.3. These results also suggest that no water is formed during the explored reaction.

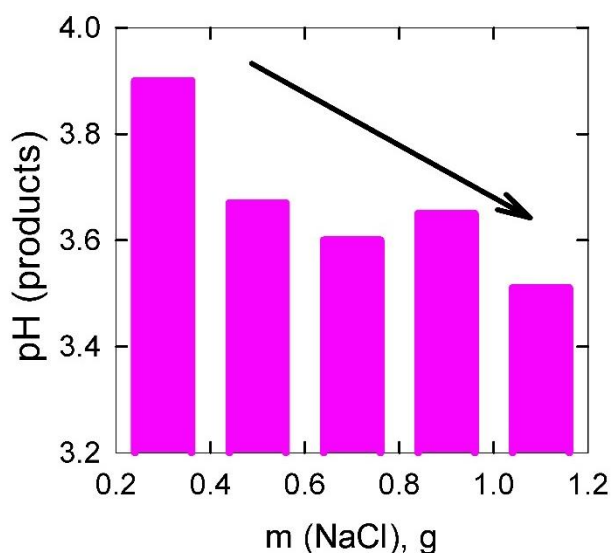


Figure 21. The increase in solution acidity is measured experimentally in the state of the products as higher amounts of NaCl catalysts are applied. The applicable error bars do not exceed 0.03 units.

6. Conclusions and final remarks

This work reports a cheap, clean, one-pot, and water-free catalyzed synthesis of DMC. The alkali salts – such as NaCl, KI, and LiI – help CH_3OH to get rid of its hydroxyl proton, which is the most kinetically challenging stage of CO_2 valorization. The favorable action of the catalyst is based on the polarization of the reactant's hydroxyl group. The strength of the catalyst is dependent on the activities of the corresponding ions. Smaller cations and anions decrease the energetic cost of the CH_3OH deprotonation more significantly. The performances of NaCl and LiCl appear to be similar, whereas KI and LiI display somewhat weaker catalytic activities. The obtained results suggest that NaCl is the most preferable component of the formulation because this catalyst is the cheapest one.

The achieved yields of DMC are hard-limited by the unfavorable thermochemistry of this reaction.^{14,31} The choice of the catalyst cannot alter this descriptor since the catalyst influences only an activation barrier. Alternative reactants must be employed to shift the equilibrium of the reaction rightward. Such reactants must be less thermodynamically stable than the current ones. For instance, a suitable derivative of an alcohol can be applied, such as an alkali metal alcoholate.

We have carried out the most comprehensive exploration of the potential energy landscape for DMC synthesis out of CH₃OH and CO₂ thus far. We unraveled two series of transition states, out of which only one is energetically realistic. By separating the integral chemical process into the constituent steps, we proved that the carboxylation of CH₃OH and the deprotonation of CH₃OH take place simultaneously. CO₂ acquires the electron from the hydrogen atom of the hydroxyl group and transforms into the carboxyl group as soon as the CH₃OH loses the proton. The protonation of the carboxyl group takes place somewhat later the proton needs to float around the CH₃OC(O)O⁻ particle following the discovered minimum energy pathway. This novel chemical knowledge is highly instrumental to further screening the catalyst for the present and similar syntheses.

The proposed synthesis of DMC appears much more convenient than the other existing options. First, the current reaction setup is very clean. Second, the reaction takes place in a single phase. Third, the need for a matrix to support solid-state catalysts has been eliminated. Fourth, the main route of synthesis does not produce water excluding the reverse reaction possibility, that is, the decomposition of an obtained product. Fifth, the properties of the reaction hold promise for its smooth extension toward higher alcohols and higher linear carbonates. The hydrocarbon radicals belonging to an alcohol R₁OH, and a promoter R₂I can be adjusted. As a result, higher symmetric and asymmetric carbonates can be synthesized, R₁C(O)OR₂.

Due to the high demand for organic carbonates and the vivid area of their synthesis, the developed catalytic scheme represents interest to a wide community of organic and physical chemists. Thanks to the demonstrated simplicity in vitro, the method may be robustly commercialized. Furthermore, the synthesis of DMC contributes to the coveted valorization of abundant CO₂ and fosters the sustainable development of humanity.

Acknowledgments

The results of the work were obtained using computational resources of Peter the Great Saint-Petersburg Polytechnic University Supercomputing Center (www.spbstu.ru). The high-performance workstation named after the prominent director Victor Belko at the School for High-Voltage Energetics belonging to SPBSTU was employed for certain applicable research and analysis procedures.

Credit Author Statement

Author 1: Conceptualization; Methodology Development; Validation; Formal analysis; Investigation; Resources; Data Curation; Writing - Original Draft; Writing - Review & Editing; Visualization Preparation; Resources; Supervision; Project administration. Author 2: Investigation; Resources; Visualization Preparation. Author 3: Investigation. Author 4: Formal analysis; Resources; Supervision.

Conflict of interest

The authors hereby declare no financial interests and professional connections that might bias the interpretations of the obtained results.

Author for correspondence

Inquiries regarding the scientific content of this paper shall be directed to Prof. Chaban at vvchaban@gmail.com.

References

1. Chaban, V. V.; Andreeva, N. A. Combating Global Warming: Moderating Carbon Dioxide Concentration in the Earth's Atmosphere through Robust Design of Novel Scavengers. LAP LAMBERT Academic Publishing, **2018**, 164 pages. isbn: 9786137327098.

2. Halder, A. K.; Ambure, P.; Perez-Castillo, Y.; Cordeiro, M. N. D. S. Turning deep-eutectic solvents into value-added products for CO₂ capture: A desirability-based virtual screening study. *Journal of CO₂ Utilization*, **2022**, 58, 101926, 10.1016/j.jcou.2022.101926.
3. Carrera, G.; Inês, J.; Bernardes, C. E. S.; Klimenko, K.; Shimizu, K.; Canongia Lopes, J. N. The Solubility of Gases in Ionic Liquids: A Chemoinformatic Predictive and Interpretable Approach. *ChemPhysChem*, **2021**, 22 (21), 2190-2200, 10.1002/cphc.202100632.
4. Nayakasinghe, M. T.; Han, Y.; Sivapragasam, N.; Kilin, D. S.; Burghaus, U. Unexpected high binding energy of CO₂ on CH₃NH₃PbI₃ lead-halide organic-inorganic perovskites: Via bicarbonate formation. *Chemical Communications*, **2018**, 54 (71), 9949-9952, 10.1039/c8cc04749a.
5. Chaban, V. V.; Andreeva, N. A.; Voroshylova, I. V. Ammonium-, phosphonium- and sulfonium-based 2-cyanopyrrolidine ionic liquids for carbon dioxide fixation. *Physical Chemistry Chemical Physics*, **2022**, 24 (16), 9659-9672, 10.1039/d2cp00177b.
6. Fajín, J. L. C.; Cordeiro, M. N. D. S.; Gomes, J. R. B. Unraveling the mechanism of the NO reduction by CO on gold based catalysts. *Journal of Catalysis*, **2012**, 289, 11-20, 10.1016/j.jcat.2012.01.010.
7. Cheng, C.; Zhu, Y.; Fang, W. H.; Long, R.; Prezhdo, O. V. CO Adsorbate Promotes Polaron Photoactivity on the Reduced Rutile TiO₂(110) Surface. *JACS Au*, **2022**, 2 (1), 234-245, 10.1021/jacsau.1c00508.
8. Ferreira, T. J.; de Moura, B. A.; Esteves, L. M.; Reis, P. M.; Esperança, J. M. S. S.; Esteves, I. A. A. C. Biocompatible ammonium-based ionic liquids/ZIF-8 composites for CO₂/CH₄ and CO₂/N₂ separations. *Sustainable Materials and Technologies*, **2023**, 35, e00558, 10.1016/j.susmat.2022.e00558.
9. Soromenho, M. R. C.; Keba, A.; Esperança, J. M. S. S.; Tariq, M. Effect of Thiuronium-Based Ionic Liquids on the Formation and Growth of CO₂ (sI) and THF (sII) Hydrates. *International Journal of Molecular Sciences*, **2022**, 23 (6), 3292, 10.3390/ijms23063292.
10. Tariq, M.; Soromenho, M. R. C.; Rebelo, L. P. N.; Esperança, J. M. S. S. Insights into CO₂ hydrates formation and dissociation at isochoric conditions using a rocking cell apparatus. *Chemical Engineering Science*, **2022**, 249, 117319, 10.1016/j.ces.2021.117319.
11. Jang, J.; Jeon, B. W.; Kim, Y. H. Bioelectrochemical conversion of CO₂ to value added product formate using engineered *Methylobacterium extorquens*. *Scientific reports*, **2018**, 8 (1), 7211, 10.1038/s41598-018-23924-z.
12. Tiwari, S. C.; Pant, K. K.; Upadhyayula, S. Energy efficient CO₂ capture in dual functionalized ionic liquids and N-methyldiethanolamine solvent blend system at elevated pressures: Interaction mechanism and heat duties. *Journal of Molecular Liquids*, **2023**, 383, 122109, 10.1016/j.molliq.2023.122109.
13. Gal, J. F.; Maria, P. C.; Yáñez, M.; Mó, O. Lewis basicity of alkyl carbonates and other esters. The Gutmann Donor Number (DN), a flawed indicator? Boron trifluoride adduct-formation enthalpy, experimentally or computationally determined, as a reliable alternative. *Journal of Molecular Liquids*, **2023**, 370, 120997, 10.1016/j.molliq.2022.120997.
14. Faria, D. J.; Moreira dos Santos, L.; Bernard, F. L.; Pinto, I. S.; Chaban, V. V.; Romero, I. P.; Einloft, S. The direct synthesis of dimethyl carbonate out of carbon dioxide and methanol is

- catalyzed by D-metals supported on various matrices. *Journal of Molecular Structure*, **2023**, 1292, 10.1016/j.molstruc.2023.136110.
15. Ma, J.; Wu, Y.; Yan, X.; Chen, C.; Wu, T.; Fan, H.; Liu, Z.; Han, B. Efficient synthesis of cyclic carbonates from CO₂ under ambient conditions over Zn(betaine)₂Br₂: Experimental and theoretical studies. *Physical Chemistry Chemical Physics*, **2022**, 24 (7), 4298-4304, 10.1039/d1cp05553d.
16. Ahmadi Goltapeh, S.; Abdolahi, S.; Jähren, J.; Miri, R.; Hellevang, H. Drivers of Low Salinity Effect in Carbonate Reservoirs Using Molecular Dynamic Simulation. *Journal of Molecular Liquids*, **2022**, 360, 119490, 10.1016/j.molliq.2022.119490.
17. Chaban, V. V.; Andreeva, N. A.; Bernard, F. L.; M. dos Santos, L.; Einloft, S. Chemical similarity of dialkyl carbonates and carbon dioxide opens an avenue for novel greenhouse gas scavengers: cheap recycling and low volatility via experiments and simulations. *Physical Chemistry Chemical Physics*, **2023**, 25 (13), 9320-9335, 10.1039/d2cp06089b.
18. Niu, Y. Q.; Liu, J. H.; Aymonier, C.; Fermani, S.; Kralj, D.; Falini, G.; Zhou, C. H. Calcium carbonate: controlled synthesis, surface functionalization, and nanostructured materials. *Chemical Society Reviews*, **2022**, 51 (18), 7883-7943, 10.1039/d1cs00519g.
19. Shayesteh, M.; Azadi Tabar, M.; Shafiei, Y.; Fakhroueian, Z.; Ghazanfari, M. H. On the adsorption behavior of a fluorochemical onto carbonate rock with the application of wettability alteration to a gas wetting condition. *Journal of Molecular Liquids*, **2021**, 326, 115031, 10.1016/j.molliq.2020.115031.
20. Schuitemaker, A.; Aufort, J.; Koziara, K. B.; Demichelis, R.; Raiteri, P.; Gale, J. D. Simulating the binding of key organic functional groups to aqueous calcium carbonate species. *Physical Chemistry Chemical Physics*, **2021**, 23 (48), 27253-27265, 10.1039/d1cp04226b.
21. Ayuso, M.; Mateo, S.; Belinchón, A.; Navarro, P.; Palomar, J.; García, J.; Rodríguez, F. Cyclic carbonates as solvents in the dearomatization of refinery streams: Experimental liquid–liquid equilibria, modelling, and simulation. *Journal of Molecular Liquids*, **2023**, 380, 121710, 10.1016/j.molliq.2023.121710.
22. Antonio González, J.; Hevia, F.; Felipe Sanz, L.; Lozano-Martín, D.; García de la Fuente, I. Thermodynamics of 2-alkanol + polar organic solvent mixtures. I. Systems with ketones, ethers or organic carbonates. *Journal of Molecular Liquids*, **2023**, 385, 122319, 10.1016/j.molliq.2023.122319.
23. Valletti, N.; Acar, M.; Cucciniello, R.; Magrini, C.; Budroni, M. A.; Tatini, D.; Proto, A.; Marchettini, N.; Lo Nostro, P.; Rossi, F. Glycerol carbonate structuring in aqueous solutions as inferred from mutual diffusion coefficient, density and viscosity measurements in the temperature range 283.15–313.15 K. *Journal of Molecular Liquids*, **2022**, 357, 119114, 10.1016/j.molliq.2022.119114.
24. Triolo, A.; Chaban, V. V.; Lo Celso, F.; Leonelli, F.; Vogel, M.; Steinrücken, E.; Del Giudice, A.; Ottaviani, C.; Kenar, J. A.; Russina, O. Oleochemical carbonates: A comprehensive characterization of an emerging class of organic compounds. *Journal of Molecular Liquids*, **2023**, 369, 120854, 10.1016/j.molliq.2022.120854.
25. Yu, W.; Maynard, E.; Chiaradia, V.; Arno, M. C.; Dove, A. P. Aliphatic Polycarbonates from Cyclic Carbonate Monomers and Their Application as Biomaterials. *Chemical Reviews*, **2021**, 121 (18), 10865-10907, 10.1021/acs.chemrev.0c00883.

26. Kalugin, O. N.; Riabchunova, A. V.; Voroshylova, I. V.; Chaban, V. V.; Marekha, B. A.; Kovrega, V. A.; Idrissi, A. In *Transport properties and ion aggregation in mixtures of room temperature ionic liquids with aprotic dipolar solvents*, Bulavin, L. A.; Chalyi, A. V., Eds. Springer Science and Business Media, LLC: 2018; pp 67-109. 10.1007/978-3-319-61109-9_5.
27. Lois-Cuns, R.; Otero-Lema, M.; Rivera-Pousa, A.; Vallet, P.; Parajó, J. J.; Cabeza, O.; Montes-Campos, H.; Méndez-Morales, T.; Varela, L. M. Mixtures of ethylammonium nitrate and ethylene carbonate: Bulk and interfacial analysis. *Journal of Molecular Liquids*, **2023**, 385, 122361, 10.1016/j.molliq.2023.122361.
28. Song, F.; Liu, L.; Wang, Y.; Fan, J.; Zhao, X. Molecular dynamic investigation on the thermophysical properties of binary molten carbonate mixtures. *Journal of Molecular Liquids*, **2022**, 363, 119922, 10.1016/j.molliq.2022.119922.
29. Uchida, S.; Sano, H.; Ozaki, H.; Kiyobayashi, T. Transport properties and solvation state of magnesium salts dissolved in propylene carbonate and γ -butyrolactone: A comparison with monovalent cation counterparts. *Journal of Molecular Liquids*, **2021**, 344, 117692, 10.1016/j.molliq.2021.117692.
30. Tatini, D.; Clemente, I.; Ambrosi, M.; Ristori, S.; Ninham, B. W.; Lo Nostro, P. Structuring effect of some salts on glycerol carbonate: A near-infrared spectroscopy, small- and wide-angle X-ray scattering study. *Journal of Molecular Liquids*, **2021**, 337, 116413, 10.1016/j.molliq.2021.116413.
31. Faria, D. J.; dos Santos, L. M.; Bernard, F. L.; Pinto, I. S.; Romero, I. P.; Chaban, V. V.; Einloft, S. Performance of supported metal catalysts in the dimethyl carbonate production by direct synthesis using CO₂ and methanol. *Journal of CO₂ Utilization*, **2021**, 53, 10.1016/j.jcou.2021.101721.
32. Vieira, M. O.; Monteiro, W. F.; Neto, B. S.; Chaban, V. V.; Ligabue, R.; Einloft, S. Chemical fixation of CO₂: the influence of linear amphiphilic anions on surface active ionic liquids (SAILs) as catalysts for synthesis of cyclic carbonates under solvent-free conditions. *Reaction Kinetics, Mechanisms and Catalysis*, **2019**, 126 (2), 987-1001, 10.1007/s11144-019-01544-6.
33. Vieira, M. O.; Monteiro, W. F.; Neto, B. S.; Ligabue, R.; Chaban, V. V.; Einloft, S. Surface Active Ionic Liquids as Catalyst for CO₂ Conversion to Propylene Carbonate. *Catalysis Letters*, **2018**, 148 (1), 108-118, 10.1007/s10562-017-2212-4.
34. Jiang, J.; Marin, C. M.; Both, A. K.; Cheung, C. L.; Li, L.; Zeng, X. C. Formation of dimethyl carbonate via direct esterification of CO₂ with methanol on reduced or stoichiometric CeO₂(111) and (110) surfaces. *Physical Chemistry Chemical Physics*, **2021**, 23 (30), 16150-16156, 10.1039/d1cp02152d.
35. Hernández, E.; Santiago, R.; Moya, C.; Navarro, P.; Palomar, J. Understanding the CO₂ valorization to propylene carbonate catalyzed by 1-butyl-3-methylimidazolium amino acid ionic liquids. *Journal of Molecular Liquids*, **2021**, 324, 114782, 10.1016/j.molliq.2020.114782.
36. Zhang, M.; Xu, Y.; Williams, B. L.; Xiao, M.; Wang, S.; Han, D.; Sun, L.; Meng, Y. Catalytic materials for direct synthesis of dimethyl carbonate (DMC) from CO₂. *Journal of Cleaner Production*, **2021**, 279, 10.1016/j.jclepro.2020.123344.
37. Deerattrakul, V.; Panitprasert, A.; Puengampholsrisook, P.; Kongkachuichay, P. Enhancing the Dispersion of Cu-Ni Metals on the Graphene Aerogel Support for Use as a Catalyst in the Direct Synthesis of Dimethyl Carbonate from Carbon Dioxide and Methanol. *ACS Omega*, **2020**, 5 (21), 12391-12397, 10.1021/acsomega.0c01143.

38. Marciniak, A. A.; Alves, O. C.; Appel, L. G.; Mota, C. J. A. Synthesis of dimethyl carbonate from CO₂ and methanol over CeO₂: Role of copper as dopant and the use of methyl trichloroacetate as dehydrating agent. *Journal of Catalysis*, **2019**, 371, 88-95, 10.1016/j.jcat.2019.01.035.
39. Zhang, M.; Xiao, M.; Wang, S.; Han, D.; Lu, Y.; Meng, Y. Cerium oxide-based catalysts made by template-precipitation for the dimethyl carbonate synthesis from Carbon dioxide and methanol. *Journal of Cleaner Production*, **2015**, 103, 847-853, 10.1016/j.jclepro.2014.09.024.
40. Choi, J.-C.; He, L.-N.; Yasuda, H.; Sakakura, T. Selective and high yield synthesis of dimethyl carbonate directly from carbon dioxide and methanol. *Green Chemistry*, **2002**, 4 (3), 230-234, 10.1039/b200623p.
41. Chen, Y.; Yang, Y.; Tian, S.; Ye, Z.; Tang, Q.; Ye, L.; Li, G. Highly effective synthesis of dimethyl carbonate over CuNi alloy nanoparticles @Porous organic polymers composite. *Applied Catalysis A: General*, **2019**, 587, 10.1016/j.apcata.2019.117275.
42. Fu, Z.; Zhong, Y.; Yu, Y.; Long, L.; Xiao, M.; Han, D.; Wang, S.; Meng, Y. TiO₂-Doped CeO₂ Nanorod Catalyst for Direct Conversion of CO₂ and CH₃OH to Dimethyl Carbonate: Catalytic Performance and Kinetic Study. *ACS Omega*, **2018**, 3 (1), 198-207, 10.1021/acsomega.7b01475.
43. Hu, X.; Cheng, H.; Kang, X.; Chen, L.; Yuan, X.; Qi, Z. Analysis of direct synthesis of dimethyl carbonate from methanol and CO₂ intensified by in-situ hydration-assisted reactive distillation with side reactor. *Chemical Engineering and Processing - Process Intensification*, **2018**, 129, 109-117, 10.1016/j.cep.2018.05.007.
44. Tan, H.-Z.; Wang, Z.-Q.; Xu, Z.-N.; Sun, J.; Xu, Y.-P.; Chen, Q.-S.; Chen, Y.; Guo, G.-C. Review on the synthesis of dimethyl carbonate. *Catalysis Today*, **2018**, 316, 2-12, 10.1016/j.cattod.2018.02.021.
45. Faria, D. J.; Moreira dos Santos, L.; Bernard, F. L.; Selbach Pinto, I.; Carmona da Motta Resende, M. A.; Einloft, S. Dehydrating agent effect on the synthesis of dimethyl carbonate (DMC) directly from methanol and carbon dioxide. *RSC Advances*, **2020**, 10 (57), 34895-34902, 10.1039/d0ra06034h.
46. Chaban, V. V.; Andreeva, N. A. Mutual miscibility of diethyl sulfoxide and acetonitrile: Fundamental origin. *Journal of Molecular Liquids*, **2022**, 349, 118110, 10.1016/j.molliq.2021.118110.
47. Chaban, V. V.; Andreeva, N. A. Mixtures of Diethyl Sulfoxide and Methanol: Structure and Thermodynamics. *Journal of Solution Chemistry*, **2022**, 51 (7), 788-801, 10.1007/s10953-022-01167-x.
48. Chaban, V. V. Diethyl sulfoxide as a novel neutral ligand in the platinum complex compound. *Computational and Theoretical Chemistry*, **2022**, 1211, 113683, 10.1016/j.comptc.2022.113683.
49. Stewart, J. J. P. Optimization of parameters for semiempirical methods VI: more modifications to the NDDO approximations and re-optimization of parameters. *Journal of Molecular Modeling*, **2013**, 19 (1), 1-32, 10.1007/s00894-012-1667-x.
50. Stewart, J. J. P. Application of the PM6 method to modeling proteins. *Journal of Molecular Modeling*, **2009**, 15 (7), 765-805, 10.1007/s00894-008-0420-y.

51. Peverati, R.; Truhlar, D. G. Performance of the M11 and M11-L density functionals for calculations of electronic excitation energies by adiabatic time-dependent density functional theory. *Physical Chemistry Chemical Physics*, **2012**, 14 (32), 11363-11370, 10.1039/C2CP41295K.
52. Chaban, V. V.; Andreeva, N. A. Sodium-ion electrolytes based on ionic liquids: a role of cation-anion hydrogen bonding. *Journal of Molecular Modeling*, **2016**, 22 (8), 172, 10.1007/s00894-016-3042-9.
53. Chaban, V. The thiocyanate anion is a primary driver of carbon dioxide capture by ionic liquids. *Chemical Physics Letters*, **2015**, 618, 89-93, 10.1016/j.cplett.2014.11.008.
54. Andreeva, N. A.; Chaban, V. V. Global minimum search via annealing: Nanoscale gold clusters. *Chemical Physics Letters*, **2015**, 622, 75-79, 10.1016/j.cplett.2015.01.026.
55. Chaban, V. Competitive solvation of (bis)(trifluoromethanesulfonyl)imide anion by acetonitrile and water. *Chemical Physics Letters*, **2014**, 613, 90-94, 10.1016/j.cplett.2014.08.066.
56. Weigend, F.; Ahlrichs, R. Balanced basis sets of split valence, triple zeta valence and quadruple zeta valence quality for H to Rn: Design and assessment of accuracy. *Physical chemistry chemical physics : PCCP*, **2005**, 7 (18), 3297-3305, 10.1039/b508541a.
57. Frish, M. J. *Gaussian 09*, Gaussian, Inc.: Wallingford CT, 2009.
58. Singh, U. C.; Kollman, P. A. An approach to computing electrostatic charges for molecules. *Journal of Computational Chemistry*, **1984**, 5 (2), 129-145, 10.1002/jcc.540050204.
59. Humphrey, W.; Dalke, A.; Schulten, K. VMD: Visual molecular dynamics. *Journal of Molecular Graphics & Modelling*, **1996**, 14 (1), 33-38, 10.1016/0263-7855(96)00018-5.
60. Allouche, A. R. Gabedit-A Graphical User Interface for Computational Chemistry Softwares. *Journal of Computational Chemistry*, **2011**, 32 (1), 174-182, 10.1002/jcc.21600.
61. Valente, A. L. P.; Riedo, C. R. F.; Augusto, F. Análise quantitativa por cromatografia. *Revista Chemkeys*, **2018**, (10), 1-10, 10.20396/chemkeys.v0i10.9602.
62. Faria, D. J.; Moreira Dos Santos, L.; Bernard, F. L.; Selbacch Pinto, I.; Carmona da Motta Resende, M. A.; Einloft, S. Dehydrating agent effect on the synthesis of dimethyl carbonate (DMC) directly from methanol and carbon dioxide. *RSC Adv*, **2020**, 10 (57), 34895-34902, 10.1039/D0RA06034H.
63. Shimizu, K.; Watanabe, M.; Canongia Lopes, J. N.; deFreitas, A. A. The heterogeneous nature of the lithium-ion diffusion in highly concentrated sulfolane-based liquid electrolytes. *Journal of Molecular Liquids*, **2023**, 382, 121983, 10.1016/j.molliq.2023.121983.
64. Thum, A.; Heuer, A.; Shimizu, K.; Canongia Lopes, J. N. Solvate ionic liquids based on lithium bis(trifluoromethanesulfonyl)imide-glyme systems: Coordination in MD simulations with scaled charges. *Physical Chemistry Chemical Physics*, **2020**, 22 (2), 525-535, 10.1039/c9cp04947a.
65. Chaban, V. V.; Andreeva, N. A. Aqueous electrolytes at the charged graphene Surface: Electrode-Electrolyte coupling. *Journal of Molecular Liquids*, **2023**, 387, 10.1016/j.molliq.2023.122724.